SQUID magnetometry from nanometer to centimeter length scales

by

Michael Jonathan Hatridge

A dissertation submitted in partial satisfaction of the

requirements for the degree of

Doctor of Philosophy

in

Physics

in the

Graduate Division

of the

University of California, Berkeley

Committee in charge:

Professor John Clarke, Chair

Professor Irfan Siddiqi

Professor Steven Conolly

Spring 2010

SQUID magnetometry from nanometer to centimeter length scales

This work was supported by the Director, Office of Science, Office of Basic Energy Sciences, Materials Sciences and Engineering Division of the U.S. Department of Energy under Contract no. DE-AC02-05CH11231.

Disclaimer

Abstract

SQUID magnetometry from nanometer to centimeter length scales

by

Michael Jonathan Hatridge
Doctor of Philosophy in Physics

University of California, Berkeley

Professor John Clarke, Chair

Information stored in magnetic fields plays an important role in everyday life. This information exists over a remarkably wide range of sizes, so that magnetometry at a variety of length scales can extract useful information. Examples at centimeter to millimeter length scales include measurement of spatial and temporal character of fields generated in the human brain and heart, and active manipulation of spins in the human body for non-invasive magnetic resonance imaging (MRI). At micron length scales, magnetometry can be used to measure magnetic objects such as flux qubits; at nanometer length scales it can be used to study individual magnetic domains, and even individual spins. The development of Superconducting QUantum Interference Device (SQUID) based magnetometer for two such applications, *in vivo* prepolarized, ultra-low field MRI of humans and dispersive readout of SQUIDs for micro- and nanoscale magnetometry, are the focus of this thesis.

Conventional MRI has developed into a powerful clinical tool for imaging the human body. This technique is based on nuclear magnetic resonance of protons with the addition application of three-dimensional magnetic field gradients to encode spatial information. Most clinical MRI systems involve magnetic fields generated by superconducting magnets, and the current trend is to higher magnetic fields than the widely used 1.5-T systems. Nonetheless, there is ongoing interest in the development of less expensive imagers operating at lower fields. The prepolarized, SQUID detected ultra-low field MRI (ULF MRI) developed by the Clarke group allows imaging in very weak fields (typically 132 μT, corresponding to a resonant frequency of 5.6 kHz). At these low field strengths, there is enhanced contrast in the longitudinal relaxation time of various tissue types, enabling imaging of objects which are not visible to conventional MRI, for instance prostate cancer. We are currently investigating the contrast between normal and cancerous prostate tissue in *ex vivo* prostate specimens in collaboration with the UCSF Genitourinary Oncology/Prostate SPORE Tissue Core. In characterizing pairs of nominally normal and cancerous tissue, we measure a marked difference in the longitudinal relaxation times, with an average value of cancerous tissue 0.66 times shorter than normal prostate tissue. However, *in vivo* imaging is required to definitively demonstrate the feasibility of ULF MR imaging of prostate cancer. To that end, we have worked to improve the performance of the system to facilitate human imaging. This is accomplished by increasing the prepolarizing field amplitude, and minimizing magnetic noise in the SQUID detector. We have achieved polarizing fields as high

as 150 mT and SQUID effective field noise below 1 fT $Hz^{-1/2}$, enabling us to demonstrate proof-of-principle *in vivo* images of the human forearm with 2 x 2 x 10 mm^3 resolution in 6 minutes.

On a much smaller spatial scale, there is currently fundamental and technological interest in measuring and manipulating nanoscale magnets, particularly in the quantum coherent regime. The observation of the dynamics of such systems requires a magnetometer with not only exceptional sensitivity but also high gain, wide bandwidth and low backaction. We demonstrate a dispersive magnetometer consisting of a two-junction SQUID in parallel with an integrated, lumped-element capacitor. Input flux signals are encoded as a phase modulation of the microwave drive tone applied to the magnetometer, resulting in a single quadrature voltage signal. For strong drive power, the nonlinearity of the resonator results in quantum limited, phase sensitive parametric amplification of this signal. We have achieved a bandwidth of 20 MHz—approximately two orders of magnitude higher than dispersive devices of comparable sensitivity—with an effective flux noise of 0.29 $\mu\Phi_0 Hz^{-\frac{1}{2}}$. This performance is in excellent agreement with our theoretical model.

To my family, and to Cate, with all my love.

Contents

List of Figures

Acknowledgments

I am indebted to a great number of people for my current success, and cannot hope to acknowledge them all. To those whose names do not appear here, my apologies, and my thanks.

This thesis would not have been possible without the continued support and tutelage of Professors John Clarke and Irfan Siddiqi, in whose labs I have worked for the past years. Together they have provided me with a variety of opportunities for hard work and education, for which I thank them. I am also grateful to them for the teams they assembled, without whom none of the work presented here would have been possible. They include Paul Reichardt, Travis Hime, Britton Plourde, SeungKyun Lee, Nathan Kelso, Whittier Myers, Daniel Slichter, Darin Kinion, Jed Johnson, Emile Hoskinson, and Ofer Naaman. We also had a number of undergraduates, including Peter Koo, Salvador Barriga, Adam Hunt, Travis Wong, and J.J. Lee who worked hard in the laboratory and made siginficant contribution to the projects they participated in. I am particularly indebted to Dr. Michael Moessle and Dr. R. Vijay, whose patient education on ultralow field MRI and dispersive rf techniques, respectively, were absolutely vital. These two fine gentlemen were not only my direct supervisors, they were boon companions and mentors, and for this I thank them from the heart. I would also like to thank Sarah Busch, who was with me from day one, through classes, teaching, and research. Her steadfast determination, friendship, and scientific and mathematical acumen helped keep me sane and moving forward. I am also indebted to Barbara Salisbury, Anthony Vitan, and Anne Takizawa who made sure I was paid and enrolled, that the paperwork was done, the lights on, and oversaw the thousand other vital details that are prerequisites for completing graduate school.

The work presented in this thesis represents a number of collaborations. Marc Shuman, John Kurhanewicz, Jeffrey Simko, Kevin Chew, Karen Chew, Lars 'the Prostate King' Schmidt all contributed heavily to designing, implementing, processing, our prostate data. Ben Inglis, Rick Redfern, and Steve Conolly all contributed heavily to the MRI project through their expertise in both conventional and unconventional MRI methodology and instrumentation.

I also thank my family, including my parents John and Susan, my brothers Trevor and Nathan, and my grandparents, aunts, uncles, cousins, and people who are not actual blood relations (especially you Stormy), but are family nonetheless. They raised me, and love me, and keep me strong. I thank my good friends Grant Miller, Jayson Stewart, and Marcus Teague for their companionship and for listening sympathetically to my complaints for literally decades at a time. Finally, I thank especially my loving wife, Cate, who continues to make my life whole and meaningful.

Chapter 1

Introduction

1.1 Magnetometry at many length scales

Information stored in magnetic fields plays an important role in everyday life. Common examples are magnetic systems for rapid storage and retrieval of information that are at the foundation of the modern information age. However, there is also a wealth of information about the natural world that is encoded in magnetic fields. This information exists at all length scales, and so magnetometry at a variety of length scales can extract useful information. Examples include exploration for natural resources at kilometer length scales, locating and mapping archaeological ruins at meter length scales, measurement of spatial and temporal character of fields generated in the human brain and heart (referred to as magnetoencephalography and magnetocardiography, respectively) and active manipulation of spins in the human body for non-invasive Magnetic Resonance Imaging (MRI) at cm-mm length scales (Fig. 1.1).

At smaller length scales, magnetometry can be used to measure magnetic objects such as flux qubits at micron length scales[1], and at nanometer length scales can be used to study individual magnetic domains, and even individual spins[2, 3]. There are many more examples of applications of magnetometry, but those illustrated here share the common feature that they all have and can be done with Superconducting QUantum Interference Device (SQUID) based magnetometer systems[4, 5]. Development of such systems for *in vivo* MRI of humans and micro- and nanoscale magnetometry will be the focus of this thesis.

1.2 SQUID fundamentals

In the phenomenon of superconductivity, pairs of electrons—known as Cooper pairs—carry a super-current without dissipation. In a Josephson tunnel junction, electron Cooper pairs tunnel coherently through a thin insulating barrier separating two superconducting electrodes (Fig. 1.2a). The magnitude of this supercurrent $I(t)$ flowing through a tunnel junction is related to the phase difference $\delta(t)$ across it by $I(t) = I_0 \sin \delta(t)$, where I_0 is the critical current. Further, in a closed superconducting loop, the magnetic flux contained in the loop is quantized in units of the flux quantum $\Phi_0 = h/2e \approx 2.07 \text{ x } 10^{-15} \text{ Tm}^2$. The two-junction SQUID, comprised of a superconducting loop interrupted by a pair of

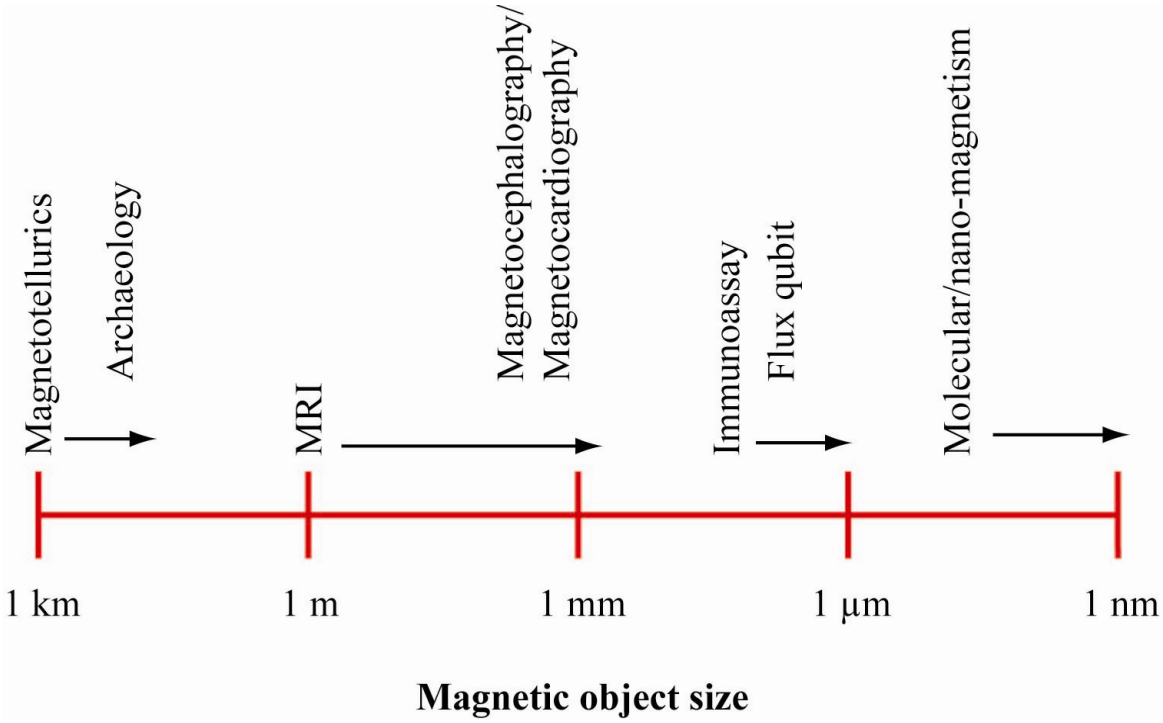

Figure 1.1: Magnetism at many length scales.

Josephson junctions (shown schematically in Fig. 1.2b), combines these two phenomena, resulting in a device with a critical current that varies with the applied flux Φ_a. For a SQUID with loop inductance $L \ll \Phi_0/2I_0$, the critical current is $I_c(\Phi_a) = 2I_0 \cos|\pi\Phi_a/\Phi_0|$[6].

In order to use this device as a magnetometer, one must first couple flux from the object of interest into the SQUID washer. For objects either much larger than or far away from the SQUID (which range from a few mm^2 to a few μm^2 in size), for instance a human head which is necessarily located a distance away from the SQUID and its typically 4-kelvin environment, a superconducting flux transformer can be used to couple flux from the object under study to the SQUID washer (Fig. 1.3a). The flux transformer consists of a wire-wound or lithographically defined input loop, sized to match the object under study, coupled to an input washer with comparable inductance fabricated above the SQUID washer.

For magnetic objects of a size comparable with the SQUID washer (few mm^2 to a few μm^2), the object can be placed directly on the SQUID washer (Fig. 1.3b), with optimal flux coupling being achieved by matching the SQUID washer size to the object being measured. For objects approaching the nm scale, this approach is no longer viable, and the magnet is coupled to the SQUID washer via a constriction in the SQUID washer (Fig. 1.3c), which can be accomplished through either a nanoscale superconducting bridge or carbon nanotube[7].

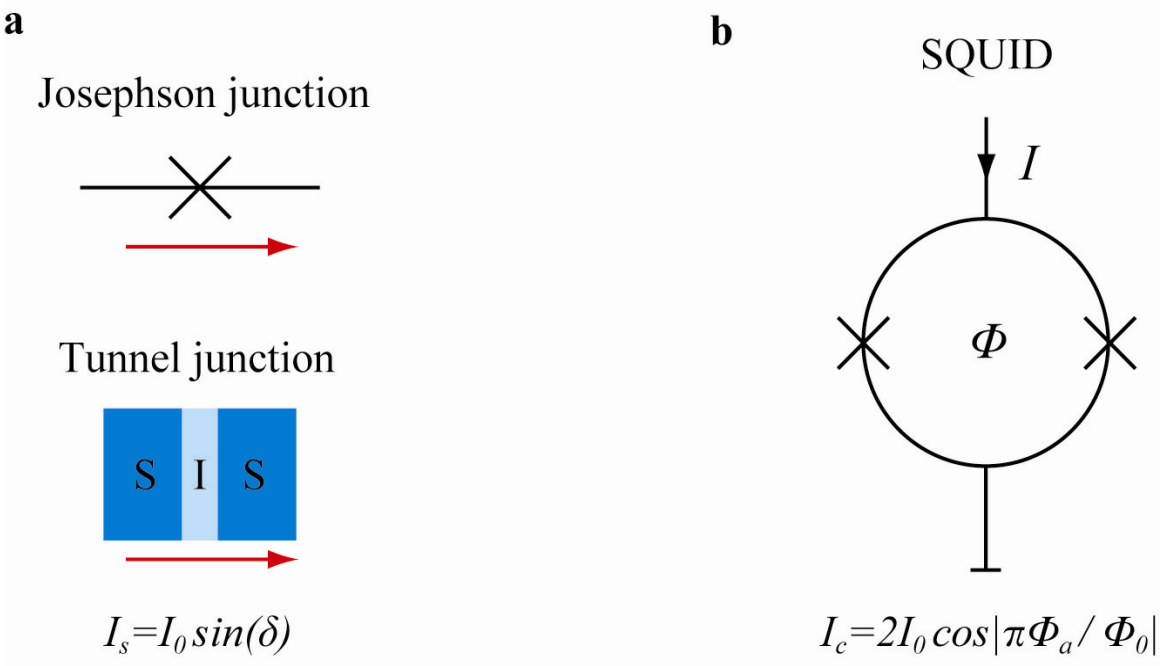

Figure 1.2: Josephson Junction and SQUID schematics. a. Schematic of josephson junction and tunnel junction. b. Schematic of SQUID.

After efficient flux coupling has been achieved, $I_c(\Phi_a)$ must be read out. The most commonly technique for SQUID readout, the so called dc SQUID readout, is accomplished by resistively shunting each junction. The device is then biased with a static current above the critical current, and the flux value is read out through the flux dependent voltage across the device (Fig. 1.4a). Often, the device is operated in a flux-locked-loop, in which flux is fed back into the SQUID washer to fix the flux value. This has the advantage of linearizing the flux-to-voltage conversion coefficient, and increasing the dynamic range of the magnetometer. Design rules for optimizing the performance of the dc SQUID are well established (31), and dc SQUIDs have achieved flux sensitivities as high as 0.02 $\mu\Phi_0$ $\mathrm{Hz}^{-1/2}$[8], and bandwidths in excess of 100 MHz, though these capabilities have not been achieved simultaneously. This technique is used in almost all geological and biomedical SQUID applications, including the ultralow field MRI technique explored in this thesis. However, the continuous dissipation in the shunt resistors produces local heating and backaction that can potentially induce relaxation and decoherence in a magnet placed directly on the SQUID.

A second method is to leave the junctions unshunted, and to read out $I_c(\Phi_a)$ by applying a ramping bias current to the SQUID and recording the current at which the SQUID switches to the normal state [1, 3] (Fig. 1.4b). It has the advantage of reduced local heating, since the SQUID is in the voltage state for only a fraction of the time. However, the flux sensitivity is significantly lower than in the resistively shunted case

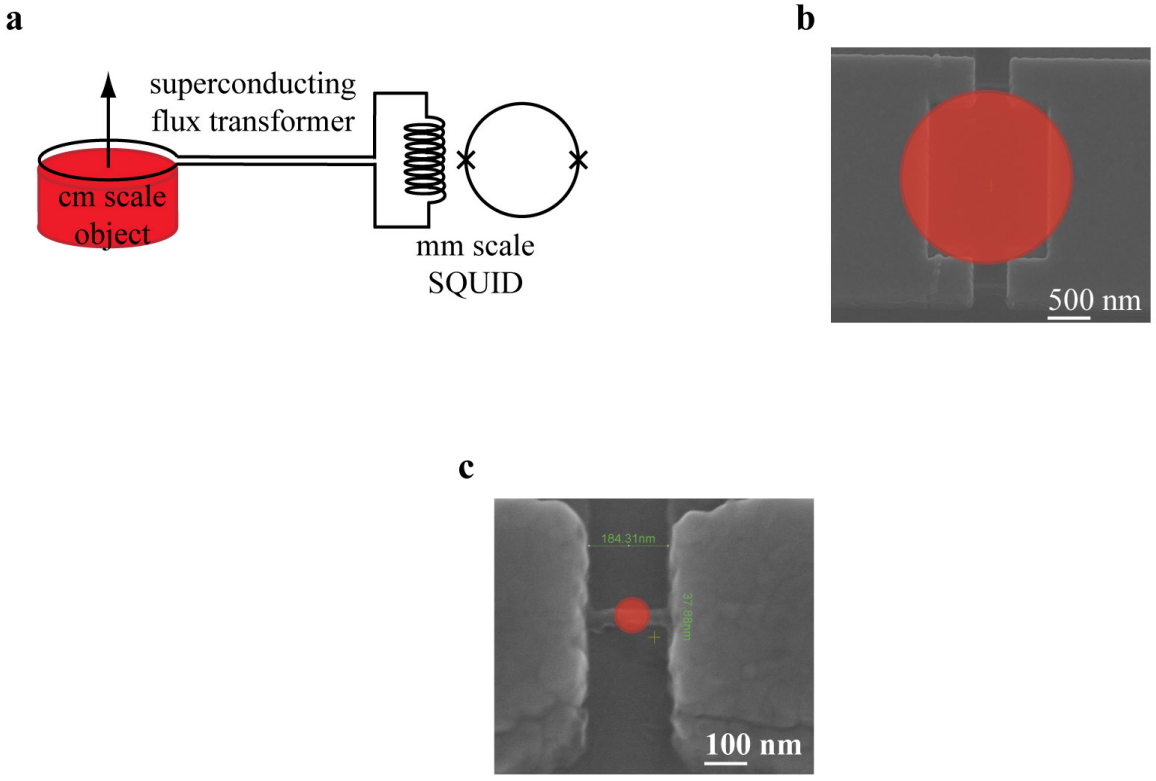

Figure 1.3: Flux Coupling Schemes. a. A cm+ scale magnetic object is coupled to a mm scale SQUID via a superconducting flux transformer. b. A micron scale magnetic object is coupled directly to a similarly sized SQUID loop. c. A sub-micron scale magnetic object is coupled to a nanoscale constriction in the SQUID loop. SEM images of devices in b-c are courteousy of Eli Levenson-Falk and R. Vijay, QNL, UC Berkeley.

because the repetition rate—and hence the bandwidth—are limited by the time (∼1 ms at mK temperatures) required for the SQUID to cool to its equilibrium temperature after returning to the zero-voltage state [9].

Alternatively, the SQUID can be operated in the superconducting regime where it functions as a flux dependent nonlinear inductor, and forms a nonlinear resonator when shunted with a capacitor (Fig. 1.4c). In this scheme, a fixed frequency microwave drive is applied to the resonator and the reflected microwave signal is demodulated. An input flux signal results in a variation of the resonance frequency and a corresponding phase modulation of the microwave drive tone. At specific bias points in the presence of a sufficiently intense drive tone, parametric amplification occurs and the flux sensitivity is enhanced. Dispersive SQUID techniques have been studied in a variety of different microwave circuit configurations over the past thirty years [10, 11, 12].

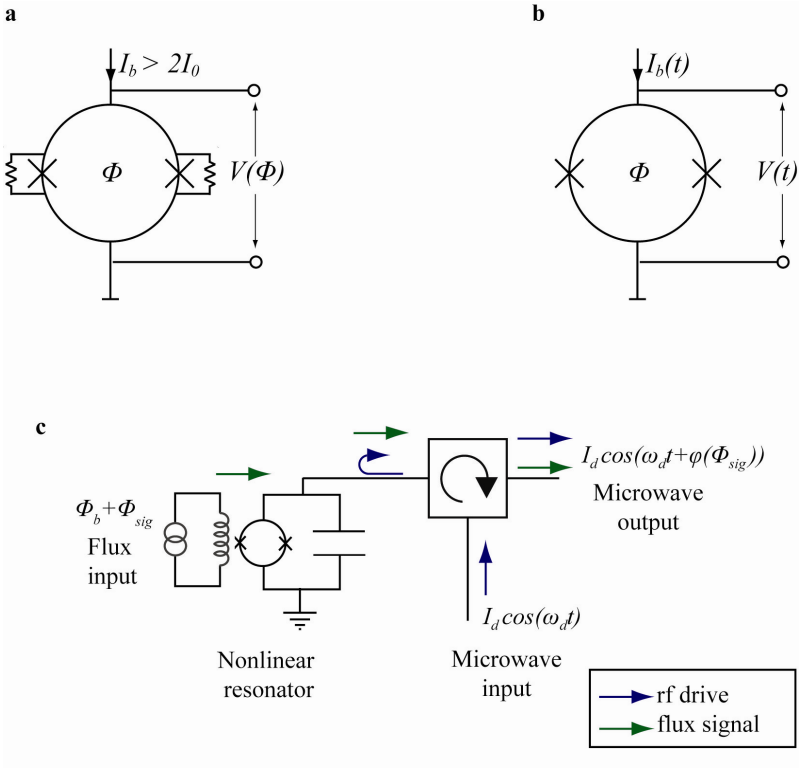

Figure 1.4: Schematics of SQUID readout techniques. a. DC SQUID readout. A resistively SQUID is biased with a static current $I_b > 2I_0$, and output is a flux dependent voltage $V(\Phi)$. b. Ramped current readout. Rapid current pulses are applied to an unshunted SQUID, and the output is the flux dependent switching current of the SQUID. c. Dispersive readout. A resonant current drive is applied to a SQUID embedded in a microwave resonator, and the flux is readout as a phase shift $\varphi(\Phi)$ of the reflected microwave drive.

1.3 SQUID as magnetometer of choice

With this array of readout and flux coupling options, there are an array of ultrasensitive magnetic measurements possible with SQUID sensors. The SQUID is extremely versatile, operating at frequencies from dc to GHz, coupling to objects from nm to km in scale, and achieving flux sensitivities at the few Bohr magneton levels in unit bandwidth, and field sensitivities better than 1 fT $Hz^{-1/2}$. However, they do have very real limitations. The need for cryogenic operation, typically at 4 K and below, adds a great deal of expense and complication. The broadband sensitivity of the SQUID is also a potential Achilles heel, as successful low noise operation requires careful shielding of the SQUID from all types of electromagnetic interference up to GHz frequencies. Thus, the general rule of thumb should be to only use a SQUID sensor if no other option achieves the required sensitivity. In this thesis I develop two such applications, ultralow field MRI (ULF MRI) for detection of cancer in humans, and dispersive GHz magnetometry for studying micro-

and nanoscale magnetometry.

While at first glance these applications seem almost entirely orthogonal, with vastly different flux coupling and readout schemes and objects under measure, they in fact share a great deal in terms of experimental techniques and guiding principles. In both applications, the primary goal is to measure precessing spins in an signal-starved environment, and both are guided by the simple requirement to maximize signal, and minimize noise. Optimizing flux coupling to the object being measured, optimizing the readout, and carefully shielding the magnetometer will be of paramount concern in each case. The primary focus of the thesis will be in the development of the magnetometers themselves, with the applications left to the theses of my fellow graduate students. In the case of ULF MRI, Sarah Busch's thesis will contain the bulk of our results in *in vivo* imaging.

1.4 MRI of human subjects, open challenges

MRI has developed into a powerful clinical tool for imaging the human body[13]. This technique is based on nuclear magnetic resonance (NMR) of protons [14, 15] polarized in a static magnetic field B_0. An applied radio frequency pulse causes the protons to precess about B_0 at their Larmor frequency $f_0 = (\gamma/2\pi)B_0$, where γ is the gyromagnetic ratio; $\gamma/2\pi = 42.58$ MHz/tesla. The precessing protons generate an oscillating magnetic field and hence a voltage in a nearby tuned pickup coil that is amplified and recorded. The application of three-dimensional (3-D) magnetic field gradients specifies a unique magnetic field and thus an NMR frequency in each voxel of the subject, so that with appropriate encoding of the signals one can acquire a complete image[16]. Most clinical MRI systems involve magnetic fields generated by superconducting magnets, and the current trend is to higher magnetic fields than the widely used 1.5-T systems[17].

Nonetheless, there is ongoing interest in the development of less expensive imagers operating at lower fields. Commercially available 0.2-T systems based on permanent magnets offer both lower cost and a more open access than their higher-field counterparts, at the expense of image signal-to-noise ratio (SNR) and spatial resolution. At the still lower field of 0.03 mT maintained by a conventional, room-temperature solenoid, Connolly and coworkers[18, 19] obtain good spatial resolution and SNR by prepolarizing the protons in a field B_p of 0.3 T. Prepolarization enhances the magnetic moment of an ensemble of protons over that produced by the lower precession field; after the polarizing field is removed, the higher magnetic moment produces a correspondingly larger signal during its precession in B_0. The ultralow field MRI system developed by the Clarke group extends the technique of prepolarized MRI to even lower precession fields[20]. Detection at these very weak fields (typically 132 μT, corresponding to a resonant frequency of 5.6 kHz) is enabled by use of dc SQUID readout, which outperforms conventional Faraday detections at low frequencies[21].

An essential component of successful MR imaging is establishing contrast between different tissue types in an image. This can be accomplished by taking advantage of differences in the T_1 and T_2 relaxation times of different tissue types. The T_1, or longitudinal, relaxation time is defined as the exponential time scale for a non-equilibrium spin population to relax to equilibrium with a longitudinal field. The T_2, or transverse, relaxation time refers to the time scale for exponential decay of a precessing spin population. An example

of T_1-weighted contrast in images is shown in Fig. 1.5, a 4 T image of the human brain, in which gray and white matter, cerebrospinal fluid, and subcutaneous fat are all distinguished by their differing T_1 values, with the tissues with shorter values being brighter.

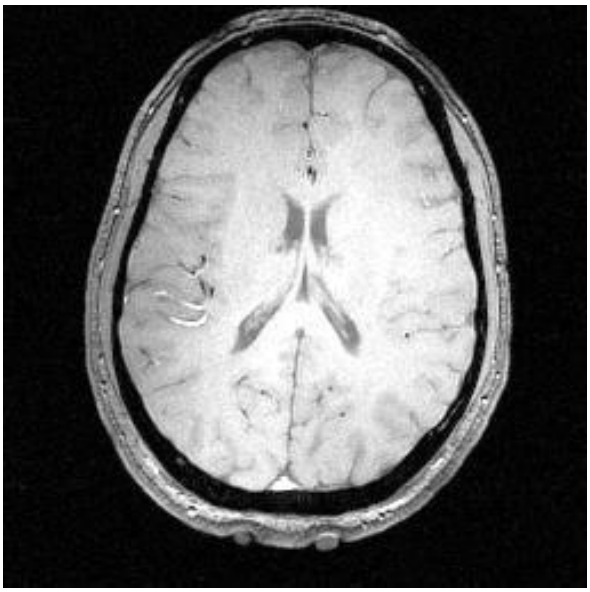

Figure 1.5: T_1-contrast image of human brain acquired at 4 T. Courteousy of Ben Inglis, Wheeler Brain Imaging Center.

An important application of MRI is the use of T_1- and T_2-contrast imaging to detect and image cancerous tissue in the body. If there is insufficient intrinsic contrast in a given tissue type, an exogenous contrast agent can be injected in order to make the cancer distinguishable. An excellent example of this is the use of gadolinium salts in the imaging of brain tumors[22]. However, there are many tissue types which do not exhibit intrinsic contrast, and effective cancer targeted contrast agents are a great challenge outside the brain. A promising alternative is to investigate the intrinsic contrast over the range of fields inaccessible to conventional MRI. Relaxometry data by Koenig and Brown indicate that below 1 mT there is potentially greater contrast, with interesting features over a range of field strengths[23]. Investigating contrast at these fields is one of the primary motivators behind the development of the ULF MRI machine, with a specific focus on imaging tumors in the human prostate, where there is no successful conventional MR imaging technique[24].

There is a further need in prostate cancer imaging for a low cost scanner which can be used to follow a tumors development over time in a 'watchful waiting' or 'active surveillance' protocol. Currently the high costs of a conventional MRI scan ($\sim$\$1000) preclude its use in these protocols, and it is hoped that the ULF MRI technique will be sufficiently inexpensive for use in this application. It also has the additional benefits of imaging in the presence of metals[25] and extremely open geometry which may allow for additional applications, such as guiding biopsy or placement of radioactive seeds in treatment of prostate cancer.

1.5 Prepolarized, SQUID-detected ultra-low field MRI

In our ULF MRI technique, we first prepolarize the imaging volume with a large magnetic field, which is then adiabatically lowered to a typically 132 μT precession field. By separating the functions of polarizing spins and providing a homogeneous precession field into two separate magnets, we can separately optimize their design. The prepolarizing magnet is designed to provide the maximum possible field strength, with an inhomogeneity of 10-20% over the imaging volume. The precession field has somewhat higher, but still rather modest inhomogeneity requirements. In order to achieve a 1 Hz line width, a relative inhomogeneity of 1 part per few thousand is required. A 132-μT field with this homogeneity is readily accomplished in our system by a Helmholtz coil. The requirements on the gradient fields are similarly relaxed. The signal is read out using a Nb flux transformer coupled to a standard 4K dc SQUID readout. In order to reject distant signal sources, the pickup coil of the flux transformer is configured as a second derivative gradiometer. Further, the dewar is custom designed to eliminate the magnetic field noise due to thermal currents in the dewar wall. A picture of the system configured for imaging the forearm is shown in Fig. 1.6.

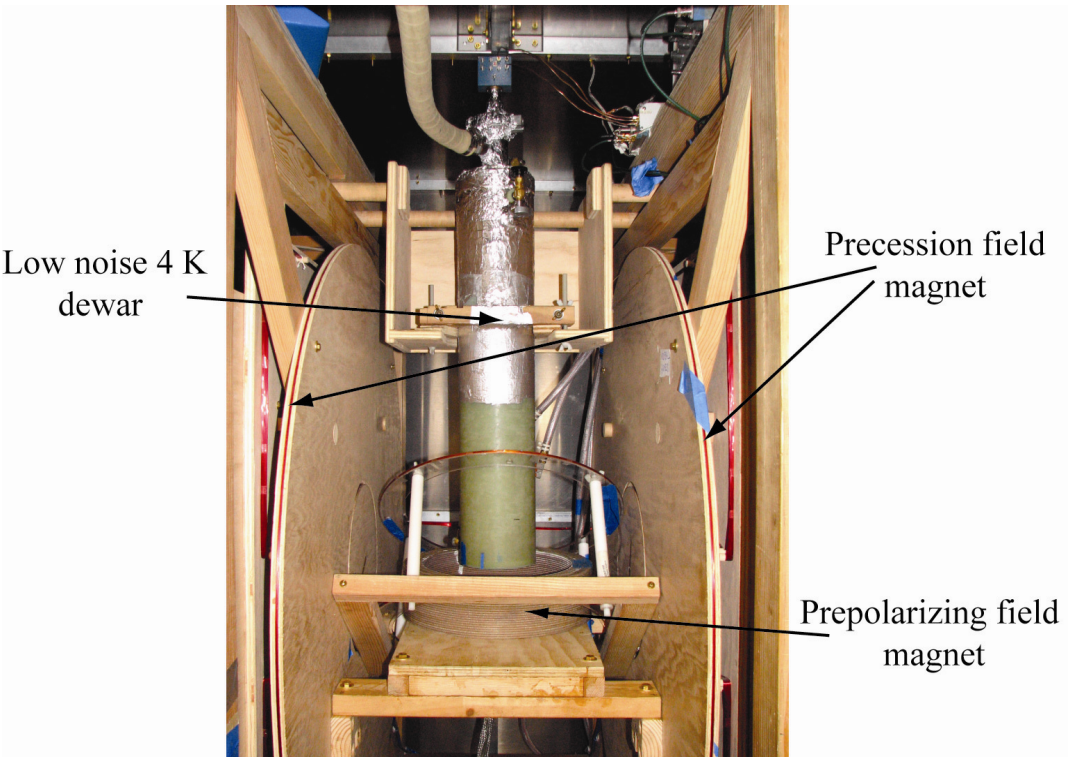

Figure 1.6: Image of ultralow field MRI system.

The key features of our ULF MRI method are prepolarization in the strongest field possible, and dc SQUID detection of the precessing spin signal with the minimum effective

field noise. These two quantities are the primary figures of merit which determine our achievable imaging speed and resolution. Over the past several years, we have increased the field strength of our prepolarizing coil from a 40 mT average field over a 6x6x6 cm^3 imaging volume to a 150 mT field. We have also made modest improvements in our readout sensitivity through the use of SQUIDs with lower intrinsic flux noise, which have allowed us to increase the effective flux noise of our readout from 2 fT $Hz^{-1/2}$ to around 0.4 to 0.6 fT $Hz^{-1/2}$. Each quantity could be improved in isolation through rather straightforward techniques. However, it is entirely another matter to operate a very sensitive SQUID in the presence of the thermal magnetic noise generated by the 30 kg current generation polarizing coil, while simultaneously tolerating 150 mT pulsed magnetic fields. Thus, emphasis is given in this thesis to the ULF MRI system development and integration, with the aim of providing practical guidance for further improvements. Attention is also given to tailoring the system for imaging of specific body parts, especially the brain and the prostate. Chapter 2 provides a more in depth introduction to NMR and MRI, and serves to introduce the particular requirements and features of SQUID-detected prepolarized MRI. It also contains an overview of the requirements for successful *in vivo* imaging of the human brain and prostate with this technique. Chapter 3 focuses on the practical development of this system, focusing in particular on development of prepolarizing coils and their associated electronics, magnetic shielding, and the integration of these two components with a sensitive SQUID detector for successful imaging. Data demonstrating the systems *in vivo* imaging capabilities are also shown. Potential further improvements and future applications are discussed in Chapter 6.

1.6 NanoSQUID for micro- and nano-scale magnetometry

In modern circuits, individual element sizes are approaching the nanoscale. Recent progress in nanoscale magnets [2] has generated excitement about using magnetic molecules for both classical and quantum information storage and processing [26, 27, 28, 29, 30, 7, 31, 32]. There is a corresponding need for magnetometer to study the dynamics of these molecular and nano-magnetic systems. Several groups are currently engaged in developing magnetometers for this purpose [3]. In these magnetometers, the magnets couple directly to the SQUID. For micron size samples, efficient coupling is achieved by sizing the SQUID loop to match the crystal. Smaller sized samples are coupled to constrictions in the SQUID washer, with the constriction ideally the same size as the magnet. Nanotubes can be used to achieve superior flux coupling[33], but are difficult to fabricate. Also, their very small critical currents can make them difficult to integrate into practical devices. Superconducting nanobridges, while substantially larger, can also be used. Both have the further virtue of tolerating the substantial transverse fields which are often required in nanomagnet measurements.

These measurements also require a readout with sufficient bandwidth ($>$ MHz) and sensitivity to measure the dynamics of few spin magnetic samples. The available readout techniques were discussed in Section 1.2. DC SQUID readout can achieve the required sensitivity and bandwidth, but local dissipation due the bias current passing through the shunt resistors makes it unsuitable for readout of magnets in direct contact with the SQUID.

Switched readout has reduced dissipation, but insufficient sensitivity and bandwidth. Dispersive readout offers minimal on-chip dissipation, and has been used in other systems to achieve acceptable flux sensitivity ([10, 11, 12]), albeit with low bandwidth. The ultimate sensitivity of this readout technique is an open question.

In this thesis, we seek to characterize the ultimate sensitivity of such a readout. A theory for tunnel-junction-SQUID based analog dispersive SQUID magnetometers is developed in Chapter 4, with the goal of establishing the bandwidth and sensitivity achievable in a practical system. Chapter 5 discusses the physical implementation of a such a device, with measurements on a tunnel junction prototype demonstrating proof of principle. In addition to demonstrating the viability of the technique for future implementation in readout of nanobridge-based SQUIDs, this device serves as an excellent micron and sub-micron scale magnetometer, with megahertz bandwidth and sensitivity suitable for measuring transitions between states in multilevel spin systems [34] and the macroscopic magnetization of spin ensembles [35].

Chapter 2

ULF MRI overview

2.1 Introduction to NMR/MRI

2.1.1 Nuclear Magnetic Resonance

The core of magnetic resonance imaging (MRI) of humans is nuclear magnetic resonance (NMR) of ^{1}H nuclei. In NMR, an ensemble of nuclei with nonzero spin are first polarized in an applied magnetic field of amplitude B_0. Spins parallel with the field have an energy $-2\mu_B B_0$ relative to spins antiparallel to the field (where μ_B is the Bohr magneton), and so the ensemble will develop a small net magnetization parallel to the applied field

$$M = N\mu_B \tanh\left(\mu_B B_0/k_B T\right) \approx N\mu_B^2 B_0/k_B T, \tag{2.1}$$

where N is the density of nuclei, k_B is Boltzmann's constant, and T is the physical temperature of the ensemble. Next, the magnetization vector is rotated away from its equilibrium direction by applying an oscillating magnetic field of amplitude $B_1(t)$ in the plane perpendicular to B_0 at the Larmor frequency $f_0 = (\gamma/2\pi)B_0$, where γ is the gyromagnetic ratio; $\gamma/2\pi = 42.58$ MHz/tesla for ^{1}H. This will rotate the magnetization vector at a rate $d\theta/dt = \gamma B_1$, where θ is measured in radians. This resonant pulse, usually referred to as an excitation pulse, can be applied with an amplitude and duration chosen to rotate the magnetization vector pulse to any desired phase relative to its equilibrium direction. The component of magnetization in the transverse plane precesses at the Larmor frequency; this rotating magnetization signal is then detected and demodulated to recover information about the spin ensemble magnetization and phase[16]. A schematic of a basic NMR experiment is shown in Fig. 2.1.

2.1.2 Effect of Gradients

Next we consider the effect of spatially varying magnetic fields on such an experiment. If we apply B_0 along the $\hat{z}$ direction, and additionally apply a linear magnetic field gradient of amplitude $G_z = dB_z/dz$, the frequencies of spins in this field will be given as $f_0(z) = (\gamma/2\pi)B_0 + G_z z$. The Fourier transform of the precessing magnetization will give a projection of the density of spins along the z-axis (see Fig. 2.2). This process of

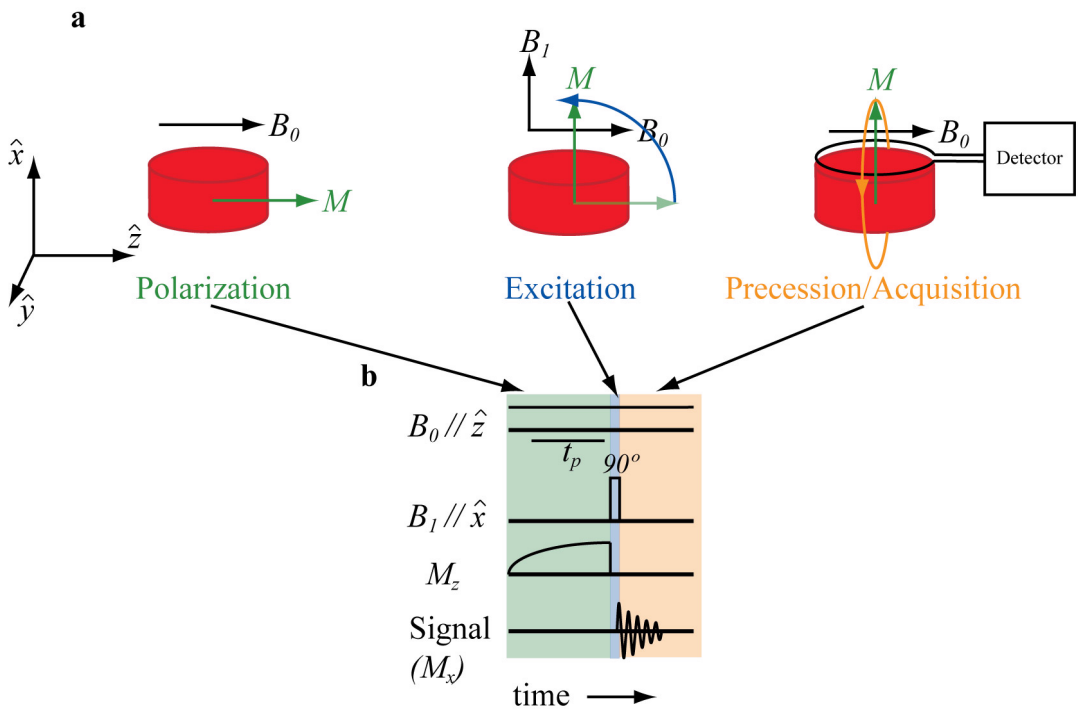

Figure 2.1: NMR schematic and pulse sequence. **a.** Schematic of the basic NMR experiment. Polarization (green) is followed by a resonant excitation pulse (blue) to tip the magnetization vector, where it precesses about B_0. In this case the x-component of the magnetization is the output signal. **b.** Pulse sequence representation of the experiment shown in part a.

encoding spatial information through the application of gradients is the heart of MRI. Indeed, if we rotate the direction of the applied gradient, for instance in the y-z plane, we can combine the information acquired through this series of projections in order to a construct two-dimensional image of the object under study. This imaging technique, however, known as projection reconstruction, is not the most efficient way of acquiring information about an object.

2.1.3 Trajectories in k-space

More useful methods of imaging 2- and 3-dimensional objects can be constructed by considering the Fourier transform of the image space. In this space, usually referred to as k-space, the real spatial information of an image is re-expressed in terms of the complex phase-number as a function of wave-vector. In this space, the origin corresponds to the coherent oscillation of all spins in the imaging region, and contains information about the total magnetization contained in a the imaging volume. At non-zero k-values, information is

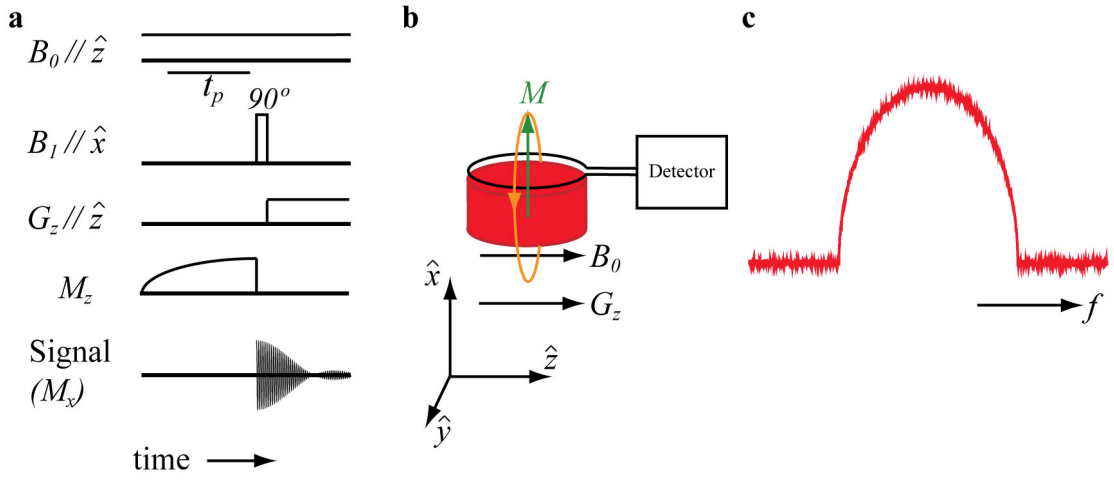

Figure 2.2: 1-dimensional projection. **a.** The NMR experiement of Fig. 2.1 is extended through the addition of a gradient G_z during the precession phase. **b.** Spins in the object being imaged (a cylinder) precess in the presence of the magnetic field with spatially varying resonant frequency $f_0(z) = B_0 + G_z z$. **c.** Fourier transform of acquired signal, demonstrating encoding of spatial information as frequency information.

encoded about higher spatial modes of the object (see Fig. 2.3 of an image and its associated k-space). Higher k-space values correspond to smaller scale information about the image space, such as edges and fine features. The importance of this representation is realized when we make the connection that applying a gradient along a direction in real space for a period of time is equivalent to scanning across k-space with a velocity $d\vec{k}/dt = (\gamma/2\pi)\vec{G}$, where $\vec{G} = \frac{dB_z}{dx}\hat{x} + \frac{dB_z}{dy}\hat{y} + \frac{dB_z}{dz}\hat{z}$. Then, acquiring signal in the presence of the 1-dimensional gradient discussed above can be understood as acquiring information along a ray in k-space starting from the origin and moving in the $+\hat{z}$ direction. By applying time varying gradients one can acquire information along any arbitrary trajectory in k-space, including lines, spirals, arcs etc. Another tool in navigating k-space is the π-pulse, in which the excitation coil is used to rotate the magnetization vector by π radians, or 180°. This has the effect of rotating the k-vector from a value $\vec{k}$ to $-\vec{k}$. The design and optimization of pulse sequences for MR imaging is a rich and complex topic; more complete discussions can be found in many MRI textbooks [16, 36]. In our ULF MRI design, we have limited ourselves primarily to simple 2- and 3-D k-space sampling methods, which are discussed in the next section.

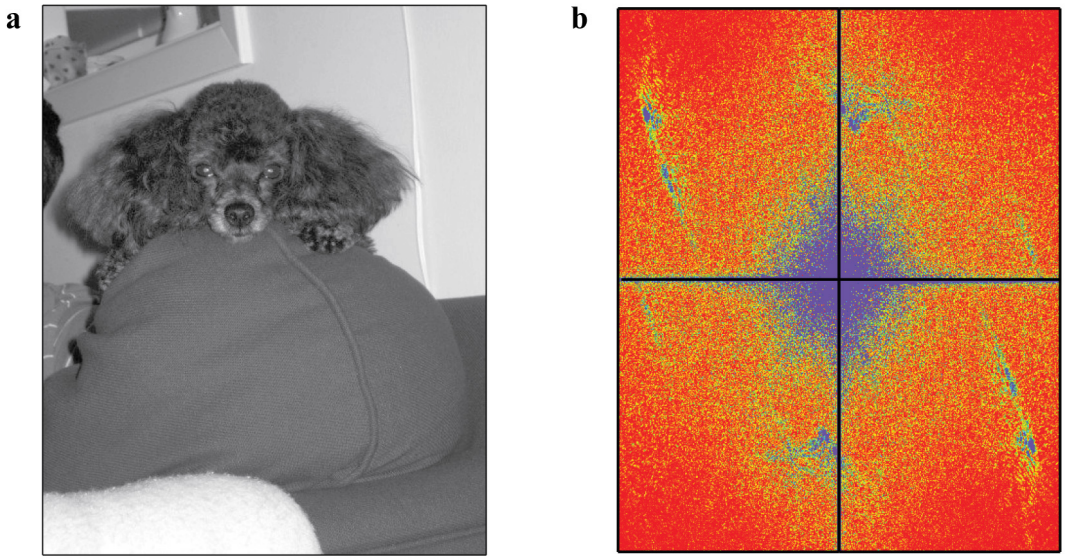

Figure 2.3: Fourier representation of an image. **a.** An image and the magnitude of its two-dimensional Fourier transform (**b**).

2.1.4 Relaxation: T_1 and T_2

The T_1, or longitudinal, relaxation time is defined as the exponential time scale for a non-equilibrium spin population to relax to equilibrium with the longitudinal magnetic field. In NMR and MRI it sets the time scale with which longitudinal magnetization develops, and hence the length of time a volume takes to polarize. The T_2, or transverse, relaxation time refers to the time scale for exponential decay/dephasing of a precessing spin population. It determines the period of time over which precessing spin population can be measured. More importantly, T_1 and T_2 can vary significantly between tissue types in the body. Thus, they can be used to distinguish tissue types, by the design of imaging sequences which weight the amplitude of each voxel according to its T_1 and/or T_2 value. An example of such weighting in MR images is shown in Fig. 1.5. An important application of MRI is the use of T_1- and T_2-contrast imaging to detect and image cancerous tissue in the body. However, there are many tissue types which do not exhibit intrinsic contrast at the 1-3 T field strengths utilized in conventional MRI. A promising alternative is to investigate the intrinsic contrast over the range of fields inaccessible to conventional MRI. Relaxometry data by Koenig and Brown indicate that below 1 mT there is potentially greater contrast, with interesting features over a range of field strengths[23].

2.2 Prepolarized, SQUID-detected ULF MRI: features

2.2.1 Separate field amplitudes for spin polarization, evolution and imaging

The pulse sequence used in our prepolarized ULF MRI technique is shown in Fig. 2.4. It is very similar to the fixed field MRI techniques discussed in the previous section, but the multiple roles of polarizing, establishing T_1 contrast, and imaging have been separated into three different field strengths, referred to as B_p, B_{evo}, and B_0 respectively. The object to be imaged is first polarized with the prepolarizing field, which is a relatively large field, typically of order 10-100 mT, with high fields strengths being desirable in order to produce stronger magnetization of the sample (see Eqn. 2.1), and hence larger signal amplitude. It is produced using a copper electromagnet, rather than a superconducting magnet as is usually the case in conventional MRI, and so can be rapidly pulsed on and off. Following prepolarization, the field strength is adiabatically ramped to a field strength $B_{evo} \leq B_p$, where the spins are allowed to allowed to relax for a period of time t_{evo}. Finally, the field is again adiabatically ramped, this time to the final field strength B_0, where standard 2- and 3-dimensional phase-encoded images are acquired.

2.2.2 Enhanced T_1 contrast at ultralow fields

Relaxometry data indicate that in many tissue types, there is potentially greater contrast T_1 at field below 1 mT, with interesting features over a range of field strengths. By varying the amplitude of B_{evo}, we can measure T_1 over a range of fields from hundreds of millitesla to a few microtesla, demonstrating both the flexibility of our imaging system, and enhanced contrast in a simple agarose gel model[37]. The enhanced contrast is due to interactions of protons in water with those bound to large, non-rotating biomolecules, and is enhanced at low field strengths. This was recently demonstrated both theoretically and experimentally in studies of agarose gels[38, 39]. Although there is not a quantitative model for such relaxation mechanisms in human tissue, it is expected that this relaxation mechanism, which is not accessed in conventional MR imaging, will provide opportunities to distinguish tissues which currently do not currently have a successful imaging method. For the past several years, this has been our primary research focus in the Clarke group, with a focus on the prostate, which currently lacks a viable conventional MR imaging technique[24]. It is important to note this ultralow field T_1 contrast does not require imaging at ultralow fields. A system similar to those designed by Connolly *et al.* at Stanford [18, 19, 40, 41] could be used with a 25-100 mT B_0 field strength.

Such a 'medium field strength' prepolarized imaging system would acquire images with identical contrast and improved SNR, at the expense of increased power consumption and substantially increased homogeneity requirements. However, for imaging of extremities, such a system would undoubtedly provide superior performance. There is a further need in prostate cancer imaging, for a low cost scanner which can be used to follow a tumors development over time in a 'watchful waiting' or 'active surveillance' protocol. Currently the high costs of a conventional MRI scan ($\sim$\$1000) preclude its use in these protocols, and it is hoped that the ULF MRI technique will be cheap enough for use in this application. It

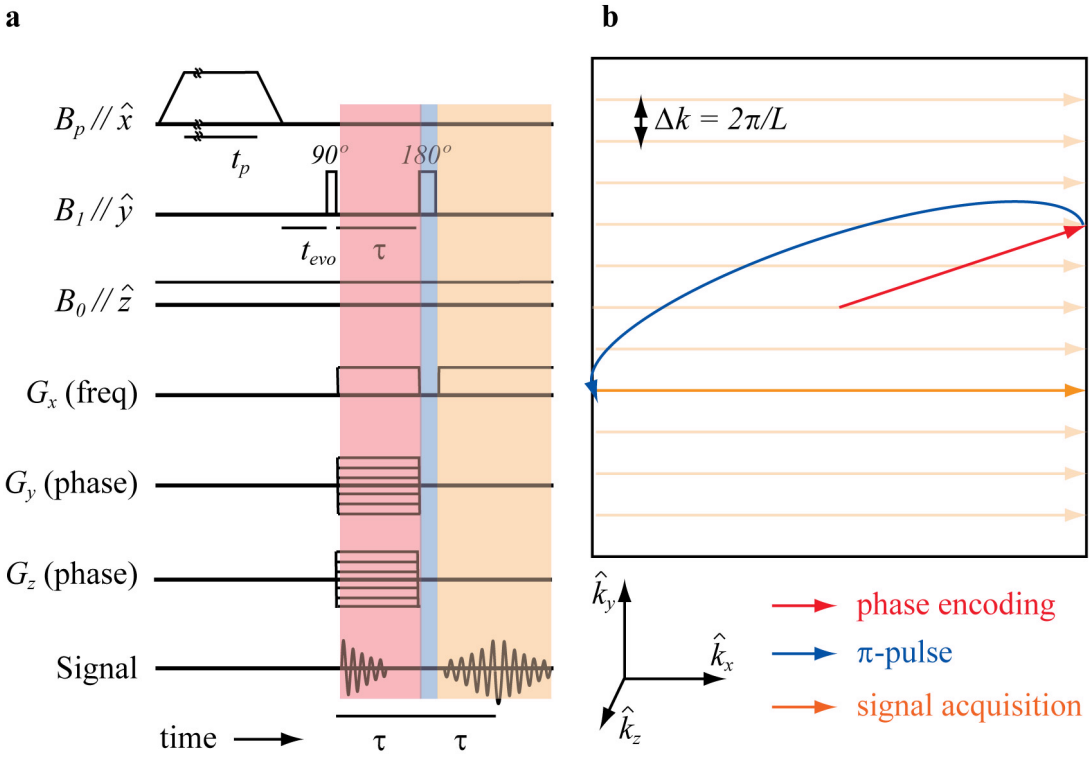

Figure 2.4: Pulse sequence for 2- and 3-d imaging. **a.** A standard ULF MRI imaging sequence. Sample magnetization is prepared by prepolarization with B_p for time t_p followed by relaxation in B_1 field for time t_{evo} to establish T_1-contrast. Imaging consists of phase encoding (red), followed by a π-pulse (blue) and acquisition (orange). By varying the amplitude of the 1 (or two) phase encoding axes, k-space can scanned in all three dimensions. **b.** x-y k-space plane. Phase encoding, π-pulse, and signal acquisition are shown as k-space trajectories. Coverage of k-space is shown as series of orange rays. The spacing of k-space lines scanned sets the field of view $L = 2\pi/\Delta k$, and the resolution $\Delta l = \pi/k_{\max}$ is set by the maximum value of k-space scanned.

also has the additional benefits of imaging in the presence of metals [25] and extremely open geometry which may allow for additional applications, such as guiding biopsy or placement of radioactive seeds in treatment of prostate cancer.

2.2.3 Untuned dc SQUID detection

Determining which combination of B_0 field strength and detection method is optimal for a given imaging application is a complicated issue. At field strengths in the 10-100 μT range, the untuned dc SQUID magnetometer is clearly the superior detection method. It has the further benefit of a flat response from dc to 100 kHz frequencies, allowing B_0 field to be varied over several orders of magnitude without altering the detector chain. At higher frequencies, it is advantageous to tune the SQUID circuit, using feedback damping to achieve broad bandwidth and excellent sensitivity[42]. At still higher fields conventional Faraday detection provides superior results. For a given geometry the sensitivity can be calculated for each method[21], but the limits of each technique at regions where they overlap is set by practical details, such as the availability of high-value, low-loss capacitors and large superconducting inductors. We have recently investigated a method for tuning our SQUID detector at 10 kHz, with potential improvements in sensitivity. The theoretical treatment and potential physical implementation will be discussed in Sarah Busch's thesis. In brief, we have constructed/purchased the necessary large inductors and capacitors required, but stability of the overall magnetometer has not yet been demonstrated.

For the purposes of our current research program, we have elected to focus on untuned, dc-SQUID detected MRI, with which we have considerable experience. For simplicity, we typically acquire images with $B_{evo} = B_0 = 132$ μT. This field strength is adequately low for enhanced T_1 contrast and very low power and homogeneity requirements for a B_0 coil large enough to allow imaging of humans. It is also high enough to avoid concomitant gradient issues over our typical sample size of 60 mm with mm resolution[43].

2.3 System overview

A schematic of our current generation ULF imaging system is shown in Fig. 2.5. The SQUID magnetometer is contained in a special ultralow noise dewar specially constructed to avoid normal metal and its associated thermal noise currents near the superconducting gradiometer[44]. The B_0 and G_x, G_y and G_z are wire wound on plywood sheets in a fixed support frame. Coils to compensate unwanted components of the Earth's field are built into the support frame. The center of the system is open, there is a 0.56 m open space between the B_0 coil halves, which accommodates the prepolarizing (B_p) and excitation (B_1) coils, as well as the object or person being imaged. The B_p and B_1 coils can be mounted in a variety of geometries; mounts have been developed for imaging hands, arms, and the back of the head, as well as for a variety of *ex vivo* specimens. Typically, B_0, B_p, and B_1 are mounted to be mutually orthogonal, as shown in the figure, to avoid undesired interactions between them.

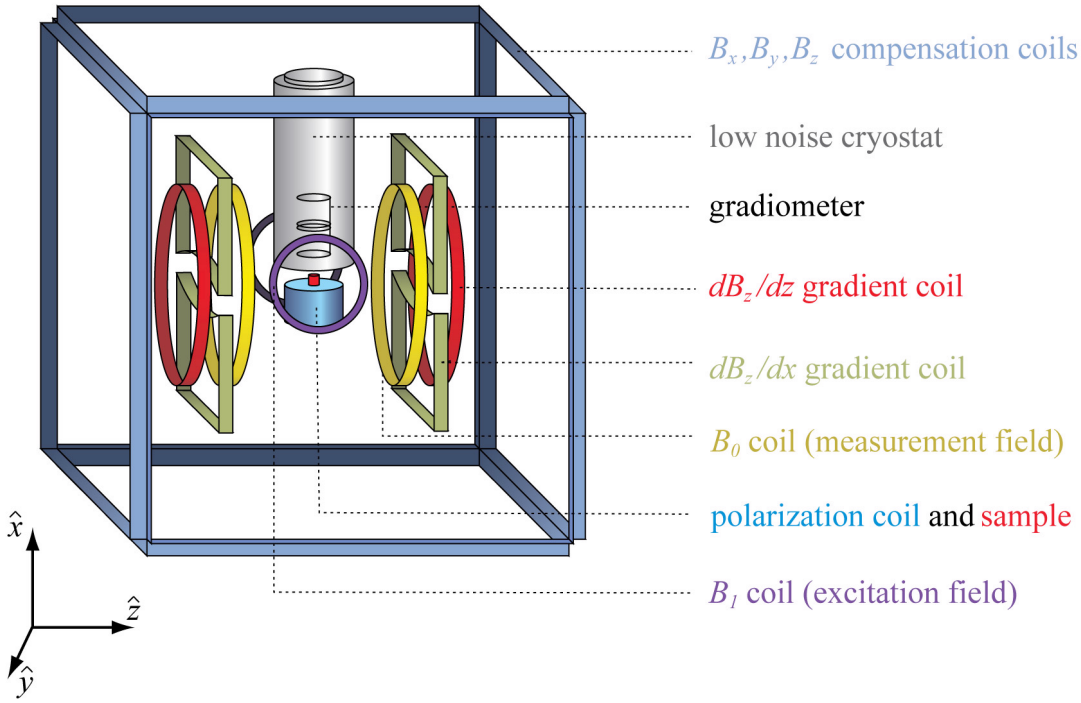

Figure 2.5: Schematic of ULF MRI system, showing the relative locations of the major elements in a typical configuration. The dB_z/dy gradient coil, which is similar in geometry and location to the dB_z/dx coil, ommited for clarity. The B_1 and B_p coils can be reconfigured at need to accomodate imaging different size/shape objects or body parts.

2.3.1 SQUID detector chain

A schematic of the components of the magnetometer is shown in Fig. 2.6. Flux from the object being measured couples to the large (63 mm) input coil, inducing a current in an similar inductance input coil tightly coupled to the SQUID washer. This allows for large objects to be coupled to the much smaller SQUID, and also allow for the SQUID to be operated in a magnetic shield (in our case a Nb can). Similar arrangements have been used for decades in biomagnetic and other applications[5]. The input coil is configured as a 2^{nd} order gradiometer in order to improve the rejection of magnetic noise from distant sources compared with a magnetometer. The object being imaged couples most of its flux to the bottom loop, allowing for imaging, but objects whose distance from the gradiometer is large compared to the gradiometer baseline of 150 mm couple the 2^{nd} derivative of the magnetic field into the input circuit, so that the overall sensitivity falls off as $1/r^5$. In the physical implementation of the gradiometer, which is wound with insulated Nb wire on a precision machined paper phenolic form, there are always imperfections in loop uniformity and orientation. Our current generation gradiometer is balanced to the part per few

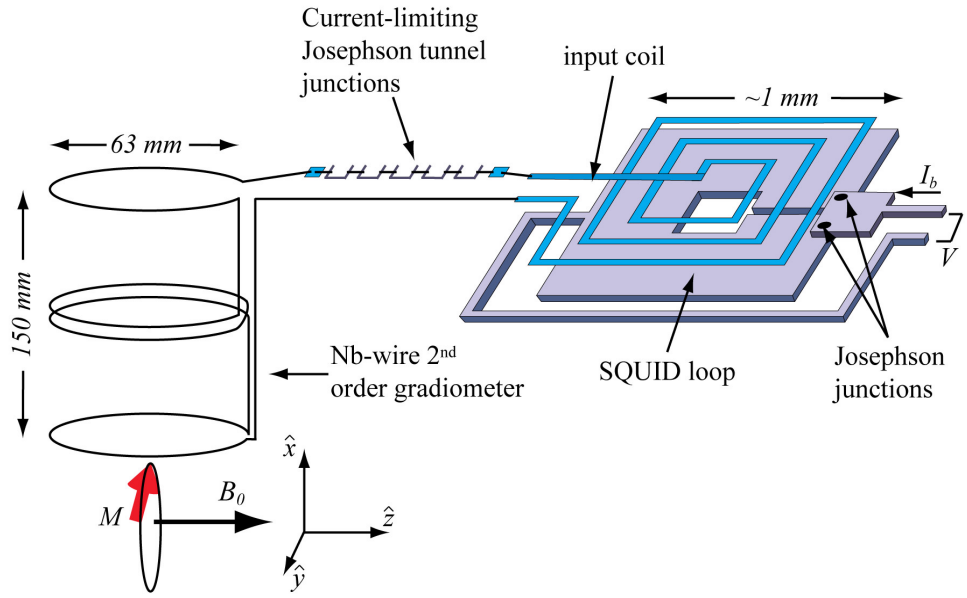

Figure 2.6: Schematic of SQUID magnetometer. The pickup coil is configured as a 2^{nd} order gradiometer in order to reject magnetic signals from distant sources. Flux from the input coil coupled to the SQUID loop with an equal inductance input coil. An array of Josesphson junctions connected in series with the pickup coil prevents currents in excess of the junctions critical currents from flowing in the circuit, and eliminates the coupling of damaging fluxes into the SQUID.

thousand level in all directions.

A second key feature of the input circuit is the array of current-limiting Josephson tunnel junctions connected in series with the gradiometer. If their critical current (10-20 μA) is exceeded due to a large flux change in the gradiometer, they switch to the normal state with a kΩ resistance, preventing potentially damaging fields from being coupled into the SQUID loop. When the current falls below the retrapping current, the junctions switch back to the superconducting state, so that the current-limiter, or 'Q-spoiler' as it is sometimes called, to functions as a self-resetting fuse in the input circuit. This allows 100 mT or greater prepolarizing fields to be positioned pointing directly into the gradiometer pickup loop, greatly easing the system design constraints.

The SQUID flux is read out using conventional flux-locked loop techniques[45]. The SQUID is biased with a static bias current $I_b > 2I_0$ and static flux $\Phi_b = \Phi_0/2$. A modulation flux is applied through to the SQUID washer with amplitude Φ_0 and frequency f_m. The output voltage, which also modulates at f_m, is amplified and mixed with a copy of the modulation signal and integrated over the cycle. The signal flux is the output of the integrator, which is fed back into the SQUID washer to lock its flux at $\Phi_0/2$, linearizing the SQUID transfer function and increasing the dynamic range. The output flux coefficient is

typically 1 V/ Φ_0, which, together with our input loop effective area of 25.4 mm^2, yields a dynamic range of $\sim$10 pT, or $\sim$ 10 nT for uniform fields. The noise level in the signal chain is set by the intrinsic flux noise of the SQUID. Our SQUIDs are produced by M. Mueck at ezSQUID Mess. und Analysegeraete, with intrinsic flux noise levels of 3-5 $\mu\Phi_0$ Hz$^{-1/2}$, and corresponding magnetic field noise levels of 0.5-1 fT Hz$^{-1/2}$.

The dynamic range of the flux-locked loop is one of the major limitations of the magnetometer, as environmental noise, such as magnetic field noise from electrical lines and equipment, can readily achieve these values. Other potential problems include spikes or level steps in the static magnetic field which occur during signal acquisition, which our laboratory neighbors regularly produce with rf equipment, laser power supplies, large pulsed magnets, etc. Also, the SQUID is vulnerable to rf frequency interference which couples to the SQUID through its leads, through direct radiation, or through the input flux transformer. To reduce these problems, the entire MRI system is surrounded with a metallic shield which screens magnetic noise from a few Hz to rf frequencies.

2.3.2 B_0, B_1, and gradients

The B_0 coil is wound using 18 gauge copper wire on a plywood frame in a Helmholtz configuration, and is powered with an Hewlett-Packard power supply in constant current mode for stability. The gradient fields are similarly wire-wound on plywood frames, with the G_x and G_y gradients as planar gradient pairs and the G_z gradient as a Maxwell pair[46]. The basic requirements of providing a static field and gradients at our precession field strength of 132 μT are very modest. The primary issues with these coils arise out of their interactions with the shield through inducing currents when pulsed on and off, and through generating magnetic field noise which couples into the magnetometer. The speed required in pulsing the gradients on and off (<1 ms) prevents filtering the gradient circuits in the range of frequencies around 5.6 kHz where detection takes place. Further, the power requirements of these coils (10s and 100s of watts) demand voltage supplies with noise that is too high for the noise requirements of the SQUID (field noise from the coil $\ll$ 1 fT Hz$^{-1/2}$). Therefore, we use mechanical relays to switch the phase encoding coils open during signal acquisition. This is not possible for the frequency encoding gradient, and so we typically power it at a fixed current throughout the experiment with a low noise, static current supply.

The B_1 field is also simply produced, typically with a wire-wound Helmholtz coil with 0.25-0.28 m radii. Excitation fields are applied with amplitudes of typically a few μT field. The time required for a $\pi/2$ rotation is given by $t_{\pi/2} = 2\gamma B_1/\pi$. This requirement, in fact, is independent of B_0, and so excitation time scales are similar at low and high fields. However, given a fixed excitation amplitude and time scale, the spectral width of the pulse is much greater at low fields. Our 5.6 kHz excitation pulses typically consist of 4-16 cycles, whereas they might consist of a 1000 or more cycles at high field. This means that slice-selection capabilities are much reduced at low fields. Further, concomitant gradient issues prevent the slice-selection gradient from being increased to counteract this effect. As a result, our minimum 'slice' is typically 20-40 mm in thickness.

2.3.3 Magnetic and rf shielding

As previously mentioned, the SQUID requires shielding against radio frequency interference, and external shielding is required to reduce the ambient flux noise at the precession frequency to below the intrinsic SQUID noise of 0.5-1 fT $Hz^{-1/2}$. It is standard in other SQUID based biomagnetic applications such as MEG and MCG to use high permeability iron and/or mu metal shields to provide this shielding. However, such shielding is not suitable for ULF MRI due to the millitesla or greater fields at the shield produced by the prepolarizing coil. Nonmagnetic metal shields can achieve excellent shielding down to frequencies of a few Hz, provided the metal plates are extremely well connected[47, 48]. In such a shield, the shielding, which is reflective at high microwave frequencies, as is usually the case in rf screened rooms, transitions to inductive shielding at lower frequencies where the wavelength of radiation becomes large on the scale of the shield[49].

At these frequencies, currents flow around the perimeter of the shield in response to applied ac fields, screening fields in the interior of the cube. This is both the source of shielding, and a major potential problem. In our current generation shield (shown in Fig. 2.7), the shield was constructed of 6-mm Al plates bolted onto aluminum square hollow tubing. In order for the shield to be both rf-tight and a good inductive shield, particular care was taken to make all connections light-tight and electrically conductive. As a result, the shield screens down to few Hz frequencies, with excellent shielding in the kHz range. However, when the polarizing coil is pulsed inside this shield, it induces currents in the shield which decay with 50 ms time scales, producing a field of around 150 μT 30 ms after the pulse at the shield center where the sample is positioned. This field is far too large for the SQUID dynamic range, and the time scale is too long for one to wait for its decay to levels where it is unimportant. It is in principle to extend the SQUID dynamic range to reach this field range, but these fields also are far too large (larger than the precession field), to be tolerated by the MRI experiment. For this reason, we are currently trying to determine the best trade off between shielding at 5.6 kHz, screening at rf frequencies, and ring down at low frequencies in these shields. Further, the shielding can be completely circumvented by noise picked up on leads connected to the various coils which connect through the cube wall. For this reason, we carefully filter and/or switch these lines open with mechanical relays, with each coil being treated according to its current, bandwidth, and operational requirements. These issues, together with our current and future planned solutions, will be discussed in Chapter 3.

2.3.4 Prepolarizing coil

The prepolarizing coil is a large electromagnet, which should provide the maximum possible prepolarizing field strength, optimally as large as a tesla, but in our experiments typically 50-150 mT. It must also be large enough to fit around or next to the object being imaged, and must be oriented in such as way as to have minimal interactions with the B_0 and B_1 coils. Also, because the coil is typically operated with 50-200 A of current, cooling of the coil, which will dissipate 10 or more kW when on, is a key requirement. It must also be ramped in a controllable fashion, particularly on the ramp-down, which should be adiabatic in order to allow for low field T_1 contrast to be developed. This requires either a

Figure 2.7: Image of current generation magnetic shield. The shield weighs approximately 1 ton, and is constructed of 6mm thick aluminum plates bolted with brass bolts to an aluminum frame.

power supply with sufficient voltage head-room to overcome the inductive kick of the coil, or some external circuit to accomplish the same task.

However, the real challenges in design and implementation of a suitable prepolarizing coil arise out of its interactions with the magnetic shielding and SQUID detector, especially in a system designed for human imaging. The first issue is noise. In our protocol, the coil is switched open during signal acquisition, to avoid coupling external noise currents into the gradiometer. However, even in the off state thermal Nyquist currents in the coil can generate significant magnetic field noise. Further, the presence of a large metal object near the gradiometer can degrade its balance, again increasing the magnetic noise which couples into the gradiometer. Additionally, the large dB/dt when the 100 mT field is turned off in 10 ms induces large circulating currents in the magnetic shield, which can exceed the dynamic range of the SQUID and require cancellation or adjustment of the shield and/or magnetometer elements to accommodate the ring down. Once an imaging target is identified, the prepolarizing coil should be designed to adequately prepolarize the arm, prostate, etc. being imaged, and the rest of the system must be designed to tolerate the prepolarizing magnet. Our experience in the design and fabrication of prepolarizing coils is addressed in Chapter 3.

2.3.5 System performance requirements

Although our ULF MRI system can achieve useful *in vivo* images, we do not achieve the levels of SNR achieved at conventional fields, which have substantially larger

polarizing fields (1.5 or 3 T in most clinical systems) and the advantage that the signal in Faraday detection scales linearly with the imaging frequency. Thus, our imaging protocols must be designed to achieve maximum SNR/time to achieve the required imaging resolution and SNR in an image in a short period of time (we limit our imaging protocols to 4 to 8 minutes). We have analyzed the requirements of efficient prepolarized imaging, and find that the most efficient method is full 3-d imaging as shown in Fig. 2.4, with the prepolarizing and imaging time scales matched to the T_1 and T_2 values of the object being imaged[46]. We have successfully this technique in imaging numerous phantoms, *ex vivo* prostate specimens, and the human arm and hand.

With the imaging protocol established, the remaining task is to maximize the signal acquisition rate through optimization of the key system parameters. The figure of merit for the system can be defined as the ratio of the product of the prepolarizing field strength and field sensitivity, expressed as $SNR/\sqrt{T_{acq}} \propto B_p/S_B^{1/2}$, where T_{acq} is the acquisition time, and where $S_B^{1/2}$ is the noise in the readout expressed as an effective field at the input of the magnetometer. The next chapter is a discussion of our efforts to maximize the figure of merit. Special attention is given to design of a system suitable for imaging the human prostate.

Chapter 3

ULF MRI system development

Given that the quantity $B_p/S_B^{1/2}$ must be maximized, in developing an *in vivo* capable system we must focus on developing the polarizing coil, the SQUID magnetometer, and the magnetic shielding in a way that is both human subject compatible and achieves high levels of performance. Unfortunately, these three systems interact strongly, and the requirements of the polarizing coil are often directly antithetical to the requirements of the SQUID and magnetic shielding. The fact that the experiment functions at all with magnetic field requirements that span 14 orders of magnitude, from the 0.1 T or greater field strength of the prepolarizing field, to the NMR fields which range from 0.1 mT to below 1 μT, to the SQUID which must achieve sub-fT $\text{Hz}^{-1/2}$ sensitivity is remarkable.

The conflicts can be sorted into three broad categories. First, there are magnetic fields which affect the spins in the MRI experiment, i.e. fields on the order of B_0, and fields with spectral content at the precession frequency. Second, saturation of the SQUID, which occurs when the total field through the SQUID exceeds either the slew rate or dynamic range of the flux-locked loop. Third, degradation of the SQUID noise performance due to either noise in the frequency band or out of band rf interference.

Fortunately, the SQUID is a robust technology, and the overall system design is simplified by the potential use of mature, commercially available SQUID systems. DC SQUIDs have been custom designed for years for biomagnetic applications, from companies such as Star Cryoelectronics, Quantum Design, and ezSQUID. Further, there are active research programs at NIST Boulder, PTB in Germany, and the MEGMRI EU project to develop more robust and user friendly SQUIDs and detector systems specifically for ultra-low field MRI applications. Thus, with the exception of tuning the SQUID detector at kHz frequencies, which was discussed briefly in Chapter 2 and will be discussed in more detail in Sarah Busch's thesis, I will consider the SQUID detector as a fixed object which we will work around. The flux-locked loop electronics are also largely a solved problem, with the possible exception of increasing the dynamic range. We have recently taken delivery of custom electronics from ezSQUID which should increase the dynamic range of the detector by a factor of 100, though we have not yet had the opportunity to integrate them into the system.

The remaining technology to be developed are the prepolarizing coil and magnetic shield. In this chapter, I will attempt to summarize the developments in these systems

during my tenure in the Clarke group, our current designs, including their strengths and weaknesses, and what I believe to be the most promising routes forward. Special attention is given to our attempts to develop technologies for *in vivo* imaging of the prostate. The chapter concludes with a summary of the fruits of our labors, highlighting some of our *ex vivo* and *in vivo* imaging results.

3.1 Polarizing coil development

3.1.1 First generation coils

Early versions of our polarizing coil were largely un-cooled, wound from 12 to 18 gauge wire, with an object (25-50 mm in size) situated in the similarly sized open bore of the magnet (a later version with peripheral cooling is shown in Fig. 3.1a). By positioning the object being imaged in such a small bore, we achieved field strengths as high as 300 mT. However, the coil had obvious shortcomings, coupling large thermal noise into the SQUID as well as only being usable for a short period of time before overheating. Further, its fringe fields were extremely weak, so that it did not provide a useful field for imaging objects which do not fit in the bore, for example any part of the human body.

They did establish the overall operation protocol. It was determined early on that the current noise of the high power supply generated unacceptably high magnetic noise which couples strongly to the gradiometer pickup coil due to their proximity. Consequently, the coil was switched open during image acquisition. Both mechanical and semiconductor relays were investigated. Semiconductor have great advantages both in speed of operation and tolerance for large currents, but were ultimately unsuitable due to the off-state leakage currents and much higher off-state capacitance which allowed high frequency noise to couple through the relay and affect the SQUID. Next, maximizing the field requires powering the coil with the maximum current which does not destroy the coil, requiring a high current power supply. Finally, the inductance of the coil results in substantial energy being stored in the coil which must be overcome in order to switch the coil off in the 10 ms time scale which is required by ultra-low field MRI. This was accomplished in these coils through a combination of switching the power supply output to its maximum negative voltage and a diode-based circuit designed to dissipate the coil energy in a resistor.

3.1.2 Liquid nitrogen cooled coil development

Several of the shortcomings of the first coils were addressed with a series of pancake coils which I'll refer to collectively as the liquid nitrogen cooled coils. The first major change, other than the obvious use of liquid nitrogen to cool the coils, was the switch from solid copper wire to Litz wire. By breaking up the metal of the coil into smaller pieces, the Nyquist noise currents are greatly reduced[50], allowing the metal to be placed in close proximity to the SQUID detector with a measured magnetic field noise level of 0.8 fT $\mathrm{Hz}^{-1/2}$. The effect of the coil on the gradiometer balance is more complicated to determine, but at least one of our gradiometers had an imbalance which was actually shimmed to a better value at certain coil-dewar spacings.

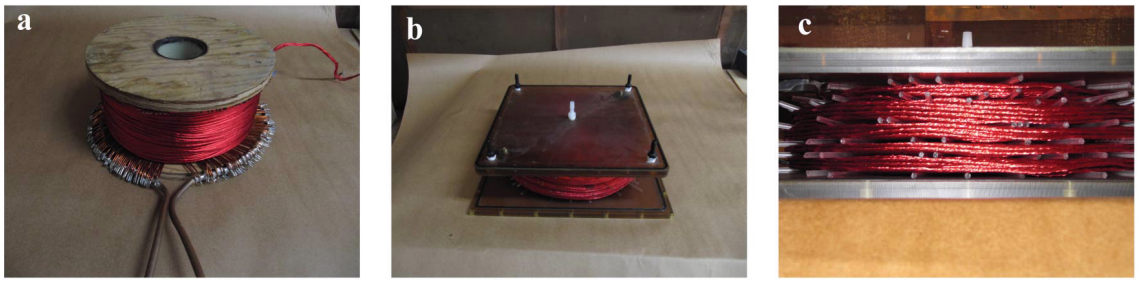

Figure 3.1: Images of early polarizing coil designs. **a.** Image of a late model open bore polarizing coil. Note peripheral cooling with copper wires and use of litz wire. **b-c.** Bottom and side views of late model LN_2 cooled coil. Coolant flows into the center, through a manifold into the channels (shown in **c)** which are held open with soft plastic sticks during winding. Each turn of wire has a cooling channel on one side to avoid formation of hot spots.

Additionally, the coil was designed to be cooled, with G-10 rods inserted in the winding process to keep channels open for cooling fluid to flow radially outward from the coil bore to drains at the periphery (see Fig. 3.1b,c). The channels, together with the larger cross section of litz wire relative to a similar resistivity copper cable, result in a lower fraction of the coil which is metallic, reducing the current density. This, together with the desire to image objects outside the magnet, shifted the geometry to a flat, pancake shaped coil. The overall coil mass consequently increased, as did the power dissipated. The total coil resistance increased to 2.5 Ω, and 40 A is used to energize the coil, resulting in 4 kW power dissipation in the coil. At this current level, the current density of the coil is approximately 5 A/mm^2.

Finally, there was the choice of coolant, namely liquid nitrogen. Somewhat ironically, cooling water was not available in our laboratory, whereas liquid nitrogen was plentiful. It worked well for these coils in a mode where we first cooled the coil to liquid nitrogen temperatures by flowing liquid through it, then stopped cooling and pulsed the coil back up to room temperature. This allows for 250 seconds of pulsing in our system, corresponding in our typical imaging sequences to 6-8 minutes of imaging. Nominally the coil can be continuously cooled while in operation, allowing for it to be pulsed indefinitely. In practice, however, this resulted in the destruction of several coils, as hot spots develop in spots where the cooling is less efficient. These spots boil liquid more rapidly, and the much lower thermal conductivity of the gas surrounding the hot spot allows it to warm still more, resulting in shorts and fires in coils where the majority of the coil is at cryogenic temperatures. Nevertheless, this coil has been very successful for us, and is well suited to *ex vivo* imaging, where the samples are small and it is very desirable to have the coil directly beneath the gradiometer. We continue to use it for our *ex vivo* prostate specimen imaging project, which is briefly discussed at the end of this chapter.

The final iteration of this type of coil was specially designed to be cooled with water, rather than liquid nitrogen. Care was taken to seal the coil well to prevent potentially

conductive water from contacting the person being imaged, and a closed system with a heat exchanger was constructed to allow manganese-doped water to be used so that the cooling water would not contribute a stray signal during imaging. The cooling channels were increased in number, and a special effort was made to make the channel distribution more uniform to prevent hot spot formation. Unfortunately, the coil was completely unusable as the self resonance frequency of the coil fell drastically when the litz wire was wet. This was attributed to inter-turn capacitance mediated by the high dielectric constant of water. As a result, the coil would ring down slowly, irrespective of the state of the switching electronics, on a time scale of seconds, preventing its successful use in imaging.

3.1.3 Large water cooled coil development

The incompatibility of litz wire and water cooling led us to look to for an alternate wire technology. The primary requirements are effective cooling and high current densities. Conolly *et al.* had successfully used square hollow copper tubing in their prepolarized MRI system, achieving high current densities and field strengths[51]. This wire, 4mm x 4mm in outer diameter (shown in Fig. 3.2a), produces excessive amounts of Nyquist noise. However, these fields fall off rapidly away from the coil, so a coil sufficiently far away from the gradiometer can be fabricated with an arbitrary cross section. We were fortunate enough to acquire an unused coil from the Conolly group which was nearly ideal for human arm and brain applications we were attempting to develop. The coil, shown in Fig. 3.2b, has inner diameter 0.324 m, outer diameter 0.413 m, and height 0.115 m. It consists of 240 turns, with an inductance of 24 mH, self capacitance 0.93 nF, 0.5 Ω resistance, and achieves 150 mT field when driven with 200 A (current density is 9.25 A/mm^2, a substantial increase over the litz wire coils).

The coil represents a substantial increase in polarizing field strength and area, but this is associated with substantial infrastructure costs. The coil dissipates 20 kW, necessitating 1-2 gallons per minute of cooling water, and the inductive kick when the coil current is switched off is nearly 1 kV. It is no longer feasible to achieve this with a linear voltage amplifier. Fortunately, the Conolly group had also developed a resonant switch technology which could be adapted to use in our SQUID based MRI system.

This switch, shown in 3.2c, is a modified H-bridge geometry with three possible current flow paths and a large capacitor in the center of the bridge. Starting with the capacitor uncharged, the Integrated Gate Bipolar Transitors (IGBTs) are biased to the conductive state, and the coil is allowed to ramp up slowly to full current with the current flowing around the capacitor. Then the IGBTs are biased off, and the current flows through the diodes and capacitor. The current charges over a quarter cycle of the resonance frequency formed by the combination of coil inductance and the capacitor, transferring the energy stored in the inductor to the capacitor. At this point, the current drops to zero and the capacitor is held isolated by the combination of IGBTs and diodes. For subsequent pulses, the IGBTs are switched back to the conductive state, the energy held in the capacitor is exchanged with the inductor, and the cycle repeats. This circuit allows the power supply to provide only the static current and power requirements of the coil.

I designed and implemented a similar version of the resonant switch, with the added

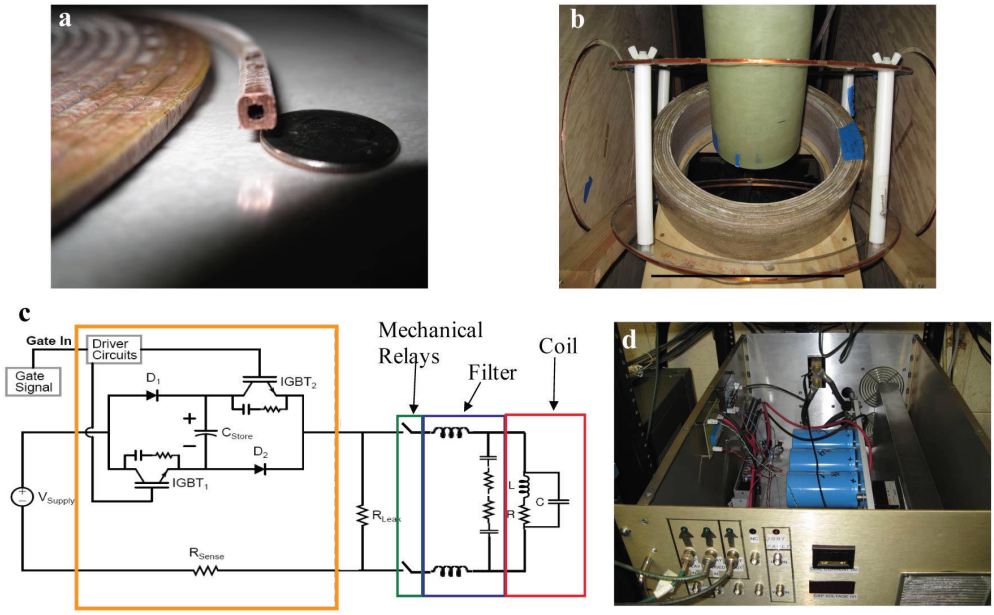

Figure 3.2: Images and schematics of water cooled coil and associated switching electronics. **a.** Image of square-hollow copper tube cross section. Quarter included for scale. **b.** Image of prepolarizing coil in the MRI system. The outer diameter of the coil is 0.413 m. **c.** Schematic prepolarizing circuit with switching electronics (orange box), mechanical relays (green) filter (blue) and coil (red) indicated. **d.** Picture of assembled switcher box. Capacitors are blue cylinders, connected to low-inductance bus (green/white bar). IGBTs and diodes are black objects visible between low-inductance bus and alunimum heat sink.

filters and switches required to make the system compatible with SQUID based MRI. The resonant frequency was designed to be 9 ms, to ensure that the rate of field change from the coil switch is less than the 20 T/s limit set by the FDA. This required a capacitance of 1.7 mF. This was achieved using three Cornell Dubilier 550CE1184 capacitors (selected for their high capacitance, low series resistance and relatively high voltage rating) in series. The series combination was necessary as the voltage rating was only 400 V per capacitor. The capacitors used were selected for matching capacitance values to avoid potentially damaging voltage redistribution effects. The IGBTs (Powerex CM300DY-28H) and power diodes (Eupec ND260N16-K) used were selected for their high breakdown voltage (1400V) and maximum current (300A) ratings. Modern IGBTs are designed to switch extremely quickly (300 ns in the model we used) in order to minimize dissipation during switching, so that there must be very little stray inductance in the circuit to avoid voltage transients which can exceed the breakdown voltage of the various components. Consequently, the core elements of the circuit were connected through a custom designed low inductance bus (custom built by Thermaflo), which can be seen in the picture of the finished circuit

(Fig. 3.2d). In order to dissipated the 20 kW dissipated by the IGBTs and diodes when the 200 A pulse is active, these elements are heat sunk on a large aluminum heat sink which is fan cooled. The IGBTs were additionally protected through the installation of RC style snubbers across them, constructed with 0.25 Ω resistance (2 Caddock MP2100-0.5 Ω in parallel), and 0.47 μF capacitance (6 Cornell Dubilier 942C16S68-F 0.68 μF in parallel). The components used and their connections were carefully designed to minimize stray inductance which can defeat the utility of the snubber. It was also a challenge to identify mechanical relays which will tolerate 200 A while also switching in a few ms. We used Gigavac model G2SP relays, which switch in around 10 ms (this becomes longer as the switches age), with two switches in parallel on both the positive and negative terminals of the coil. These switches are actually intended for high voltage applications, but seem to be holding up well in our application. Most switches explicitly rated for 100 A or greater currents are motor/generator contactor style switches, and their switching times and isolation properties are completely unsuitable. A mercury or equivalent wetted switch would be ideal due to their extremely low contact resistances, but I was unable to identify a commercial product with the needed properties.

The IGBTs are controlled with the Powerex's purpose built IGBT driver circuit (BG2A), and the switching signal is provided by a logic circuit which integrates a number of interlocks together with both manual and computer external controls. One interlock connects to a water flow meter (Proteus Industries 203C24) mounted in series with the cooling water line downstream from the coil; flow drop below the set threshold switches the coil off and prevents further pulses. Another interlock internal to the switcher box measures the electrical current returning from the coil, and prevents the mechanical relays from being opened unless the current flowing through the coil is less than an amp. A third is mounted with the mechanical relays, and prevents the coil from being switched on if the relays are open. The current is provided by a MagnaPower TS200-125 switched-style power supply, operated in constant-voltage mode. The high efficiency of the supply is very desirable in order to decrease the total power required by the experiment. However, its internal semiconductor switches generate a substantial 8 kHz signal as well as broadband current noise even which is transmitted through the switcher box and relays even in the off state. This was addressed through the addition of an LCR filter installed in a shielded box just outside the mechanical relays. The inductors were constructed by winding 4 gauge wire (Flexaprene #4 heavy weld cable) on ferrite cores (Fair Rite # 5943018701). The large wire tolerates the 200 A pulse, and at these current values the ferrite is strongly saturated and contributes minimally to the coil inductance. When the current it switched off the ferrite recovers, and the element acts as an inductor.

The whole system has been installed and functioning in our laboratory for the past year. It functions very well, and the whole coil plus associated electronics contribute around 0.5 fT $\mathrm{Hz}^{-1/2}$ to the overall system noise (with the majority being due to Nyquist currents in the coil), and, once configured, reduces the control of the polarizing coil to a single TTL line, with the interlocks protecting the subject being imaged and the operator from sequence design error and/or component failure. The coil however, has proven to be incompatible with our current generation shield. Due to its much larger size, it generates a much larger EMF than the liquid nitrogen cooled coil, generating fields in the shield walls

which ring down with the time constants of the cube (discussed in the next section). The field at the center due to shield ringdown is as high as 150 μT at the sample location 30 ms after coil shutoff, and the longest time constant of the ring down is 50 ms. Even with active cancellation using a separately installed magnetic coil to reduce it to 1-10% of this value, this remains far too large for both the SQUID and the MRI experiment to tolerate. This has necessitated a redesign of the magnetic shield.

Despite these difficulties, and the increased power and circuit design requirements, we believe this technology is the best solution for future *in vivo* imaging systems. The primary limit on the field size produced is related to the size of the coil and the static power dissipation and the voltage rating of the switching circuit. It is also possible that a different square-hollow tube geometry could achieve a higher current density than we use in our current coil, which would allow for a higher field without increased inductance. In principle, coils with power dissipation of 100+ kW and switching voltages of several kV can be operated with readily available commercial components.

The general rules of thumb when designing polarizing coils of this type are to keep the bore as small as possible (as the field/amp-turn scales as 1/a, where a is the turn radius), and to keep each turn as close to the object being measured as possible (so that the coil cross sections remains roughly square). Furthermore, the object being measured *must* be located in the bore of the magnet, or at worst at or very near the face of the magnet. The price paid in terms of power and coil switching voltage for polarizing much outside the bore of the magnet is substantial. With this in mind, we propose a so-called 'one-sided' configuration for future prostate and other *in vivo* imaging targets (shown in Fig. 3.3), in which the polarizing coil is mounted concentrically around the gradiometer, and the coil and dewar are placed against the lower abdomen of the subject being imaged. In this case, the coil should have as small an inner radius as possible, subject to the constraint that it not raise the SQUID noise level either through its Nyquist noise currents or through disrupting the gradiometer balance. One should add turns until the required field can be achieved, optimizing the contribution of each turn by keeping it as close to the imaging target as possible.

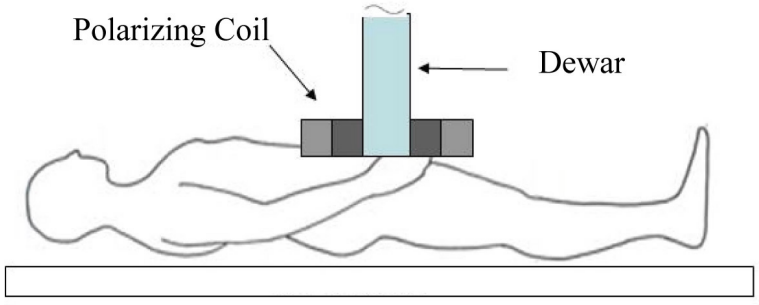

Figure 3.3: Schematic of proposed prostate imaging configuration. The prepolarizing coil and dewar are arranged concentrically, directly above the lower abdomen.

3.2 Shield development

For successful SQUID operation, the gradiometer must be shielded from noise at both the imaging frequency and radio frequencies. In most SQUID based biomagnetism applications, the magnetic shield of choice is a mu-metal screened room. These have superior shielding performance, screening frequencies from rf down to a few Hz[5]. However, they are also extremely expensive, heavy, and, most importantly, easily polarized by large magnetic fields, rendering them unsuitable for our application.

An alternate technique for shielding is the use of a thick non-magnetic metallic shield. Aluminum is typically the metal of choice for such shields due to its light weight, good conductivity, and low cost. Such shields have been used for decades, and achieved adequate low frequency shielding[47, 48]. Such rooms are constructed from solid aluminum sheets of 1.5-20 mm thickness, either welded or bolted together to form a continuous electrical connection across the entire surface of the shield. The mechanism of shielding in these rooms changes as a function of frequency and conductivity between the sheets (see Fig. 3.4). At high frequency the shield acts as a typical Faraday shield, with electromagnetic radiation reflecting from the surface of the cube. In this scenario, only the metal within a few skin depths of the surface actively participates in shielding, and the most important factor in achieving good shielding is avoiding cracks, seams, and holes in the shield which can allow radiation to penetrate the shield. Large penetrations in the wall can be accommodated without admitting rf radiation by the use of long cylindrical waveguides whose fundamental modes are at high frequencies (typically 10 GHz or higher). All frequencies below the fundamental are attenuated as they propagate down the waveguide[52].

At lower frequencies, the wavelength becomes larger, eventually exceeding the dimensions of the shield. In this limit, the entire shield (Fig. 3.4b) or individual plates of the shield (Fig. 3.4c) act as inductive elements, screening ac magnetic fields incident on them through induced currents[49, 53]. This mode is entirely dominant in the kHz frequency range. Whether the screening in a shield is due to currents in individual plates depends on the spatial location of the field source (sources close to individual plates primarily produce fields in those plates), and the plate-plate resistance. In welded aluminum rooms, this distinction is eliminated if the welds are properly constructed[47, 48].

3.2.1 Development of 1-ton cube

Our current magnetic shield is a cube 2.44 m on a side constructed of 6 mm thick 5052 alloy aluminum plates on a conducting support frame made from 38 x 38 mm^2 square hollow tubing (see Fig. 3.5). Great care was taken to connect the plates electrically through use of bolts every 150 mm to the aluminum frame, and the joints and seems are constructed to avoid seams which can admit rf radiation. The door is similarly constructed, with BeCu coated steel rf-fingers being used to seal perimeter of the door in the closed position. Water feed lines and other large cables are fed into the cube via 12-25 mm diameter by 160 mm copper and brass wave guides to avoid degrading the rf shielding. The shield weighs in total around 1000 kg, and is carefully sited to minimize the most common perturbations to the Earth's field, which in our lab are due to the nearby freight elevator and its iron counterbalance, in the plane transverse to the B_0 field.

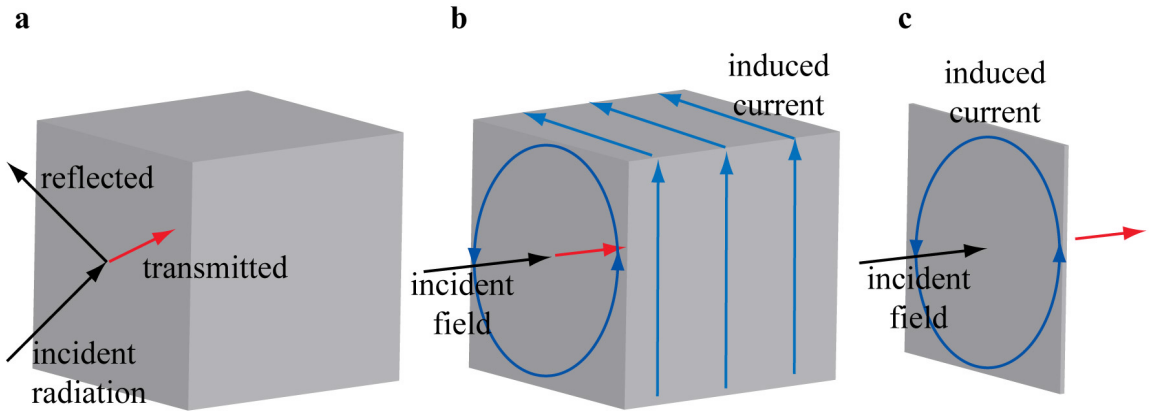

Figure 3.4: Illustration of magnetic shielding at different frequencies. **a.** High frequency reflective shielding. The incident radiation, with wavelength much less than the cube dimensions (gray cube), reflects from the cube wall, and a small portion is transmitted. **b.** Low frequency inductive shielding for cube-shaped shield. The incident field, with wavelength much greater than the cube dimensions, induces currents that flow throughout the perimeter of the cube and screen the field inside the cube (shown in red). **c.** Similar to **b.** with shielding accomplished by a single plate. Induced currents screen field transmitted through plate.

The shield, or 'the cube' as we refer to it, has excellent rf and low frequency shielding properties. Noise from electrical devices, especially at 60 Hz and its odd harmonics, which had previously been a major nuisance is greatly attenuated, indicating that the shield operates down to frequencies of at least a few 10s of Hz. In addition to the prepolarizing coil relays and filters, which are mounted in aluminum boxes bolted directly to the cube wall, we have additional cast-aluminum enclosures where signals such as the excitation and gradient pulses are fed through mechanical relays and then through the cube wall to BNC mounts on the inside. These have worked well in reducing noise contributions from power supplies and amplifiers that are not needed during signal acquisition. We have recently experimented with adding LC filters and ferrite beads as additional high frequency and rf shielding on the input lines, though it is not yet apparent if these are effective. The cube itself is grounded through a direct connection to earth (via water pipes which enter the ground a few feet from the connection point), and we are (un)fortunate enough to be below the water table, so the ground connection is excellent and far less noisy than connecting to the power ground.

The primary problem with the cube is associated with its being such a good low frequency shield. As we have moved to higher prepolarizing fields and physically larger polarizing coils, the interactions of the coil with the cube have increased. This results in large currents being induced in the cube as a whole, as well as in each individual plate.

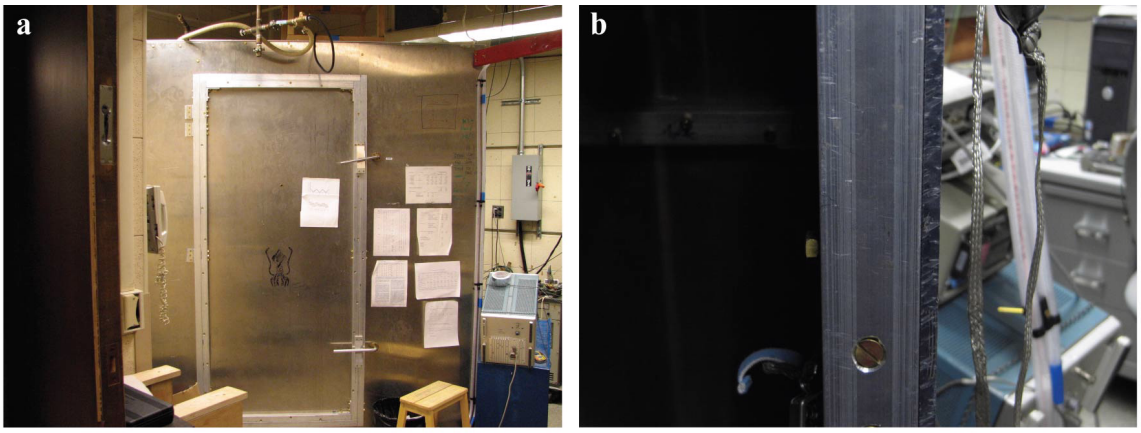

Figure 3.5: Images of 6mm aluminum shield. **a.** View of front of aluminum cube with door shut. Cube is 2.44 m on a side. **b.** Close up of door frame, showing how plate (right) is connected to aluminum frame.

When the water-cooled coil is pulsed at full strength, the induced currents in the wall produce a field as large as 150 μT along the B_p field axis 30 ms after pulse turn off. By measuring the fields at the wall, Koos Zevenhoven and Fredrik Öisjöen, were able to map the current distribution in the walls as a function of time after the polarizing pulse. They found that the polarizing pulse excites both currents in each plate and currents which flow coherently around the cube. The time constant was measured to be 50 ms for the longer lasting coherent current. They also found that the current bends around the door, which is less well connected electrically, pushing current up into the ceiling and down into the floor.

We can cancel the emf somewhat through the use of a coil mounted around the belly of the wooden MRI frame. This allows us to reduce the field measured by the SQUID to 1-10 % of the uncancelled value, but this is still too large for MRI, and its decay time is comparable to the decay times of tissue at 100 μT fields, so we cannot out wait it. We have also investigated using the SQUID output to dynamically cancel the field in the vertical (MRI $\hat{x}$ direction). This successfully allowed the SQUID to remain locked even after uncompensated full power pulses. However, as the SQUID measures the 2^{nd} derivative of magnetic field, not the field itself it is not clear whether cancelling the gradient field due to the asymmetric current in the cube wall is equivalent to cancelling the field itself, and any $\hat{y}$-component of the field is not cancelled at all.

3.2.2 Next generation shield

Consequently, we are also constructing a next generation shield to investigate strategies for magnetic shielding in the presence of a large prepolarizing coil. We used our SQUID detector to measure the ambient kHz range noise in the laboratory in a copper mesh room, which provides rf shielding but presumably no kHz shielding, and found the ambient field noise in the room to be on the order of 1 fT $\mathrm{Hz}^{-1/2}$, with occasional spikes of 10 fT

$Hz^{-1/2}$ spikes due to local sources. In such an environment, we need only modest amounts of kHz shielding to allow our 0.5-1 fT $Hz^{-1/2}$ SQUIDs to operate unimpaired by external noise. The goal, then, is to develop a shield which has only modest (say 10x shielding over the 4-7 kHz frequency range), and time constants on the order of a ms, which would allow the residual field to decay quickly enough not to hamper the MRI experiment. The new shield must also retain its rf screening properties, but this is only a modest requirement.

Our strategy is to eliminate the long-timescale coherent shielding effects by electrically isolating each individual plate. We are also making the plates thinner to shorten their response time. Theoretical and experimental results from the late 1980s indicate that individual plates can act as effective shields[53], though the use of multiple plates in our shield and the indeterminate nature of the magnetic noise sources confounds a simple calculation of the effects. In fact, modest screening can actually increase the noise contribution from a distant noise source. This is because distant noise sources are already strongly screened by the gradiometric nature of the input coil, and so a nearby shield which may disrupt the homogeneity of the field from a distant source by a larger factor than it reduces its amplitude can actually make the situation worse. Further, the most likely noise sources tend to be at an intermediate distance (say 1-10 m away in our laboratory and neighboring laboratories) where their interactions with the shield and gradiometer are both moderately inhomogeneous, further confounding simple design rules. Finally, even if successful, incorporating shielding designed to provide the minimum necessary shielding for a specific location is not a general solution to the problem, as the previous 1-ton cube was intended to be.

Nevertheless, such a shield can serve as proof of principle and allow our research to proceed. We have recently constructed a next-generation 1.6 mm thick 6061-alloy aluminum shield to test these ideas (see Fig. 3.6). The frame is wooden, and each plate is deliberately electrically isolated from its neighbors. Also, the overall design is intended to be more symmetric, with the plate patterning mirroring the presence of the door in each of the other three sides. RF shielding is accomplished through use of non-conductive-adhesive backed aluminum tape, which seals the seams against rf without connecting the plates at low frequencies. Preliminary measurements indicate that the time scale has been reduced to 6 ms in the new shield, which is longer than optimal, but perhaps tolerable, depending on the extent to which the magnitude of the field has also decreased. The rf shielding also appears to be adequate. We can modify the connection between the plates through the use of conductive-adhesive backed aluminum tape and aluminum bridges between plates, and are currently investigating the effect of the plate-plate conductivity. Another question under consideration is whether the plates can be bridged with large value capacitors, which might give a sharper frequency response than resistive connections. Details of these measurements will be available in Koos Zevenhoven's Master's thesis, to be published at Aalto University, Helsinki, Finland.

3.3 Applications and capabilities

In this section I will briefly summarize some of our imaging results with the current generation imager. The details of the earlier images have been published in Dr. Whitter

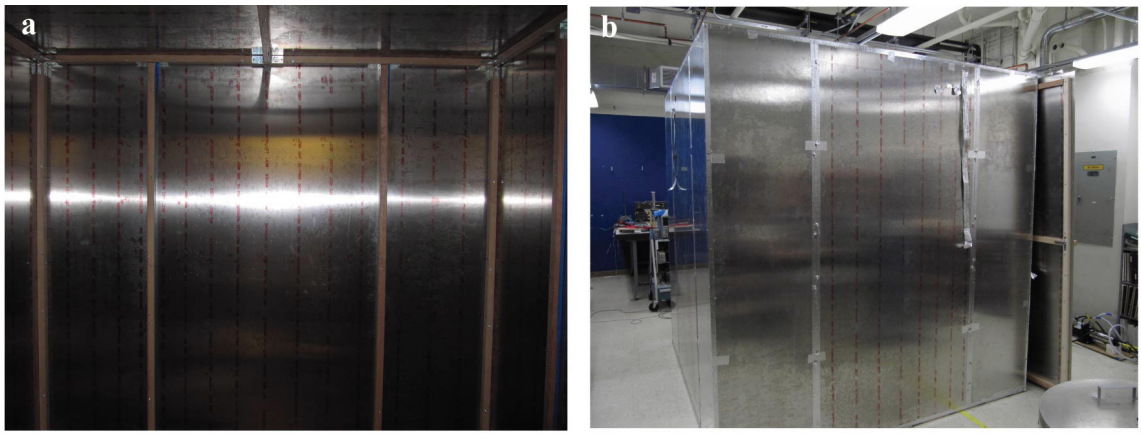

Figure 3.6: Images of 1.6 mm aluminum shield. **a.** Photograph of interior of 1.6 mm aluminum shield, showing wooden supports. **b.** Photograph of exterior of 1.6 mm aluminum shield. The 4 vertical walls are designed to be symmetrical to avoid disorting the shield response to the prepolarizing pulse.

Myers' thesis[46], and newer results are to be the subject of Sarah Busch's forthcoming thesis. Our two main scientific goals have been to investigate ultralow field T_1 contrast as a mechanism for identifying tumors which are not visible to conventional MR imaging techniques, with our research focused primarily on imaging of human prostate cancer, and the general ability of our scanner to achieve *in vivo* images of humans.

3.3.1 *Ex vivo* prostate cancer results

We are currently conducting a study on ultralow-field T_1-contrast in *ex vivo* prostate tissue in collaboration with Dr. Jeff Simko and the Comprehensive Cancer Center Tissue Core the UCSF. This research was classified as human subjects exempt under protocols CPHS 2005-5-55 (UCB) and 180-H05 (LBNL). We have currently measured T_1 in 30 pairs of de-identified prostate tissue specimens. Each sample consisted of two tissue specimens, each nominally 5x5x1 mm^3, but with sizes varying from approximately 3x3x1 mm^3 to approximately 10x10x2 mm^3. Expert visual inspection judged one specimen to be nominally normal tissue and the other nominally cancerous tissue. The samples were acquired immediately after surgery at UCSF, and were selected from regions of the prostate not needed for patient care. The specimens were sealed in a biohazard bag, placed on ice and transported to UC Berkeley for NMR measurements. The bag was placed in a polystyrene holder between the prepolarizing coil and the dewar, and measurements were made 2-6 hours after ligature. Throughout the experiment, the specimens were maintained at 4 °C to slow degradation.

For each sample, we conducted NMR with a weak gradient along $\hat{z}$ to separate the samples in frequency space. For each sample a number of averages were acquired at either 10 or 20 low field evolution time (t_{evo}) points spanning 200 ms, and used to

determine an average value of T_1 for each sample. Occasional system instabilities caused a fraction (approximately 10%) of the acquisitions to have high noise. These traces were readily identified, and were removed from the averaging. We plotted the decay of the signal magnitude from each specimen versus t_{evo}. The resultant exponential decay was least squares fit to the function $y(t_{evo}) = Ae^{-t_{evo}/T_1} + y_0$. The offset y_0 was defined using the average noise 100 Hz off-resonance from the NMR peaks. After the MR imaging session the specimens were frozen on dry ice and returned to UCSF, where they were formalin-fixed, processed, sectioned, and their histology determined. In particular, each sample was labeled by the histologist by the estimated fraction of the sample that was tumor.

Our results show that there is strong T_1-contrast between normal and cancerous prostate tissue in these samples, though there is significant variation in the T_1-values from sample to sample. However, given each pair of specimens with T_1 values T_{1A} and T_{1B}, we can express the contract C between them in an image as $C \propto e^{-t_{evo}/T_{1A}} - e^{-t_{evo}/T_{1B}}$. We can further define the time of maximum contrast as $t_{evo}(C_{\max}) = \ln(T_{1B}/T_{1A})/(1/T_{1A} - 1T_{1B})$. If we assume that the T_1values are similar, it is convenient to redefine $T_{1B} = T_{1A}(1-\delta)$, where δ is small. Then, combining the above expressions, we find that $C \propto \delta = 1 - T_{1B}/T_{1A}$. Thus, we can use δ as a figure of merit for contrast in an optimized image. This figure of merit is plotted vs. difference in percentage tumor for each sample pair in Fig. 3.7.

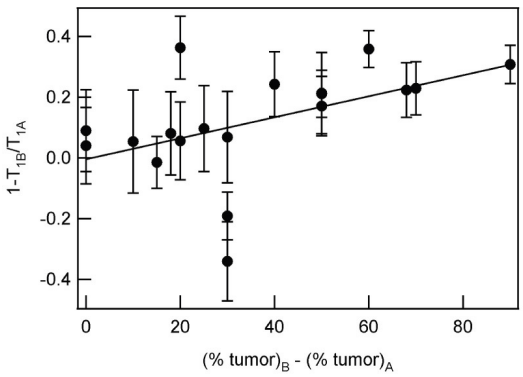

Figure 3.7: Plot of 1-T_{1B}/T_{1A} versus percentage difference in tumor content for *ex vivo* prostate specimens. The data were acquired with B_0=B_{evo}= 132 μT, on freshly excised prostate specimens held at 4° C.

This plot clearly shows that, in most cases, the specimen with more tumor has a lower T_1. There is a clear trend of δ upward with increasing tumor percentage difference. The least squares linear regression y=-0.004 + 0.0035x, with a correlation coefficient of 0.49. This correlation passes nearly through (0,0), indicating that, on average, the specimens pairs with similar tumor content have similar T_1 values. Extrapolating this line out to 100% difference in percentage tumor results in $\delta = 0.34 \pm 0.16$. On average, therefore, we conclude that T_1 of 100% tumor is 0.66 times shorter than 100% normal prostate tissue. If we remove the 3 outliers (case # 7,14,17) under the assumption that the tumor content was not represented accurately by the section on which the histology was performed, the linear

regression gives y = 0.0231 + 0.0034x with a correlation coefficient of 0.86. This results in $\delta = 0.37 \pm 0.06$.

This preliminary study has several limitations. An ongoing difficulty was the fact that T_1 appeared to change with time over a period of a few hours, presumably because the tissue began to decay. This decay both limited the time over which we could average the data and prevented our studying the dependence of T_1 on the evolution field B_{evo}. We limited our measurements to $B_{evo} = 132$ μT, but since T_1 may well depend on B_{evo} it is quite possible that a different choice could yield higher contrast. Furthermore, the fact that BPH and tumor have similar T_1 values is a potential complication for in vivo diagnoses. It is possible, however, that different values of B_{evo} would result in distinct values of T_1 in these tissues. Another issue is that, to slow deterioration of the tissue, all of our specimens were maintained at about 4 °C. We do not know how the T_1 values will change at body temperature. We suspect that this limitation can be overcome only with *in vivo* studies.

3.3.2 *In vivo* imaging results

Figure 3.8 shows an image representative of our last generation imaging capabilities. It is an image of a 10 mm thick slice of the human forearm, acquired as part of a three-dimensional image with the pulse sequence shown in Fig. 2.4, and a total imaging time of 6 minutes. It was acquired with an average prepolarizing field of $B_p\,(avg) = 40$ mT across the arm with a liquid nitrogen cooled coil. The magnetic field noise was approximately 1.5 fT $\mathrm{Hz}^{-1/2}$, and the in plane resolution was 2 x 2 mm^2. This arm image was acquired under human subjects protocols 180-H04 (LBNL) and CPHS 2005-1-41(UCB).

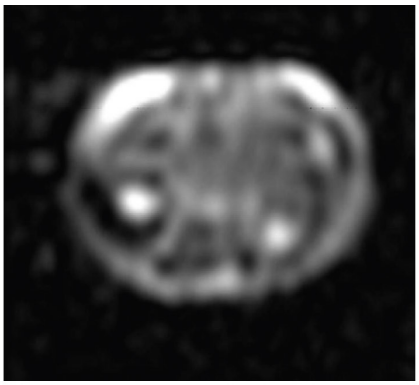

Figure 3.8: ULF MRI image of the human forearm, acquired with $B_0 = 132$ μT, $B_p\,(avg.) = 40$ mT, and $S_B^{1/2}$= 1.5 fT $\mathrm{Hz}^{-1/2}$.

Unfortunately, many of the recent improvements in SQUID noise, prepolarizing field, and shielding which would allow us to demonstrate higher quality images have not yet been combined in a system capable of, and approved for, human imaging. In particular, when we are able to successfully integrate the new water-cooled coil into the system, the polarizing field will be a factor of 4 higher for this image, with a uniform 150 mT applied

across the entire slice. Further, we have experienced SQUID noise levels approximately a factor of 2 lower than the noise in the displayed arm image. With these changes, the figure-of-merit for the image would be a factor of 8 higher, allowing for either an 8 fold reduction in voxel size (say to 1 x 1 x 5 mm^3), or 8 fold SNR increase, or some combination thereof. Realizing this improvement is the team's major focus in the coming months. We are also working with corporate partners to acquire funding for further development of *in vivo* prostate imaging systems based on these same technologies.

Chapter 4

Micro- and nanoscale magnetometry

4.1 Introduction

A quite separate application pursued during my tenure at Berkeley has been developing magnetometers for micro- and nanoscale magnetism. Such magnetometers are desirable for several applications. Among them are the increasing numbers of nanoscale magnetic elements used in modern hard drives, and recent progress in nanoscale magnets [2], which has generated excitement about using magnetic molecules for both classical and quantum information storage and processing [26, 27, 28, 29, 30, 7, 31, 32]. Several groups are currently engaged in developing magnetometers for this purpose [3]. In these magnetometers, the magnets couple directly to the SQUID. For micron size samples, efficient coupling is achieved by sizing the SQUID loop to match the crystal. Smaller sized samples are coupled to constrictions in the SQUID washer, with the constriction ideally the same size as the magnet. Nanotubes can be used to achieve superior flux coupling[33], but are difficult to fabricate. Also, their very small critical currents can make them difficult to integrate into practical devices. Superconducting nanobridges, while substantially larger, can also be used. Both have the further virtue of tolerating the substantial transverse fields which are often required in nanomagnet measurements.

These measurements also require a readout with sufficient bandwidth ($>$ MHz) and sensitivity to measure the dynamics of few spin magnetic samples. DC SQUID readout can achieve the required sensitivity and bandwidth, but local dissipation due to the bias current passing through the shunt resistors makes it unsuitable for readout of magnets in direct contact with the SQUID. Switched readout has reduced dissipation, but insufficient sensitivity and bandwidth[4].

Alternatively, the SQUID can be operated in the superconducting regime where it functions as a flux dependent nonlinear inductor, and forms a nonlinear resonator when shunted with a capacitor. The magnet flux threading the SQUID loop is read out by applying a fixed frequency microwave drive to this resonator and demodulating the reflected microwave signal. An input flux signal results in a variation of the resonance frequency and a corresponding phase modulation of the microwave drive tone. At specific bias points in

the presence of a sufficiently intense drive tone, parametric amplification occurs and the flux sensitivity is enhanced. Dispersive SQUID techniques have been studied in a variety of different microwave circuit configurations over the past thirty years [10, 11, 12]. Recent work on the dispersive readout of superconducting qubits—single, pseudospin 1/2 systems—also harnesses the nonlinearity of the Josephson junction to boost sensitivity, but typically these devices are operated in the bistable regime as digital detectors [54, 55, 56].

My project, conducted under the joint supervision of Irfan Siddiqi and John Clarke, has been to develop an analog magnetometer with megahertz bandwidth suitable for measuring transitions between states in multilevel spin systems [34] and the macroscopic magnetization of spin ensembles [35]. A theory for the performance of this device is developed in the remainder of this chapter. Experimental results for a prototype tunnel-junction magnetometer are presented in Chapter 5.

Depending on the operating conditions, the performance ranges from an effective flux noise of 0.14 $\mu\Phi_0\mathrm{Hz}^{-\frac{1}{2}}$ and 0.6 MHz of signal bandwidth to a noise of 0.29 $\mu\Phi_0\mathrm{Hz}^{-\frac{1}{2}}$ and a bandwidth of 20 MHz. Moreover, our device exhibits quantum noise limited sensitivity, and is a general purpose amplifier suitable for a variety of dispersive measurements. These results are in quantitative agreement with our theoretical model which, in particular, predicts that low flux noise and wide bandwidth are obtained for a low resonator Q (quality factor). The theory allows us to optimize our device for specific applications, and provides insight into the fundamental and practical limitations of a single, two-junction SQUID operated in a dispersive regime.

4.2 Requirements

Although nanoscale magnetometers do not appear to share many features with the ULF MRI system developed in previous chapters, both devices are driven by common requirements. Each device must achieve efficient flux coupling to the object under study, and be read out with the highest sensitivity possible in a environment actively hostile to successful SQUID operation.

4.2.1 Flux coupling

At the micron scale, efficient coupling can be achieved by matching the SQUID loop diameter to the object under study and placing the object directly over the SQUID loop (see Fig. 1.3b). However, at the nanometer scale, this is no longer feasible. At these length scales coupling is achieved by fabricating a SQUID with a constriction in the washer on the scale of the object to be measured (see Fig. 1.3c). Such constriction are in fact a type of Josephson junction, and can be used either as merely flux coupling elements if their critical current is much higher than the SQUID junctions, or can themselves form the SQUID junctions. Although varieties of constriction junctions (often referred to as micro- or nanobridge junctions depending on their size) have been in use for decades, precise understanding of their current-phase relation and critical current is an open problem. Further, measurement of molecular magnets, an ultimate goal in our current research efforts, requires nanobridges whose widths are as small as possible, presenting a challenge to reproducible

and controllable fabrication. These issues are the focus of a separate project at QNL[57], and will be a major topic of Eli Levenson-Falk's thesis. In this thesis we consider the case of a tunnel-junction based SQUID, which limits the magnetometer to micron to few hundred nanometer scale magnetic objects, with the overall experimental and theoretical framework are intended to serve as proof-of-principle and test-bed for future nanobridge SQUID magnetometers.

4.2.2 Operation in strong magnetic fields

Further, nanoscale magnetism experiments are typically conducted in the presence of static magnetic fields on the order of a tesla in strength. Such field strengths are not compatible with standard tunnel junctions, as substantial flux threads the junction cross section, and affects the junction performance. Nanobridge junctions, with their tolerance for much stronger magnetic fields, are thus doubly desirable, and indeed are the junction technology of choice in micro- and nanoscale SQUID magnetometers[3].

4.2.3 High bandwidth, low dissipation readout

As previously mentioned, however, the read-out techniques typically used in these magnetometers do not achieve the desired speed and sensitivity. In order to conduct measurements on a small spin-ensemble with coherence times at the microsecond time scale, readout with ideally many MHz of bandwidth and few-spin sensitivity is desired. We believe that such levels of sensitivity can be achieved through the use of a dispersive SQUID readout, which has the added virtue of minimal on-chip dissipation which can affect the dynamics of spins closely coupled to the SQUID washer.

4.3 Theory of Dispersive Magnetometer

4.3.1 Circuit model

We model our device as a lumped element parallel resonator, as shown in Fig. 4.1a. Incoming and outgoing microwave signals from the resonator are separated using a circulator. Although we eventually intend to construct magnetometers using nanobridge junctions, we have developed the theory for a tunnel-junction SQUID. This has the advantage of an ideal and robust current-phase relationship, will enable quantitative comparison of the theoretical sensitivity with fabricated magnetometers, and can be readily extended to a nanobridge SQUID with known current-phase relation.

The resonator is inherently nonlinear due to the inclusion of a Josephson junction as its inductive element. When weakly driven with an external microwave tone, the resonator response is linear. At higher drive amplitudes, the response becomes nonlinear, and the resonator dynamically bifurcates into one of two oscillation states past a critical bias condition. This effect has been used as the basis for a digital detector for qubit measurements[58]. Moreover, at a bias slightly below the critical point the nonlinear resonator can be used as a doubly degenerate parametric amplifier[59, 60, 61]. We are interested in determining the magnetometer performance in both the linear and nonlinear

regimes, and we will show in subsequent sections that parametric amplification plays an important role in the ultimate flux sensitivity.

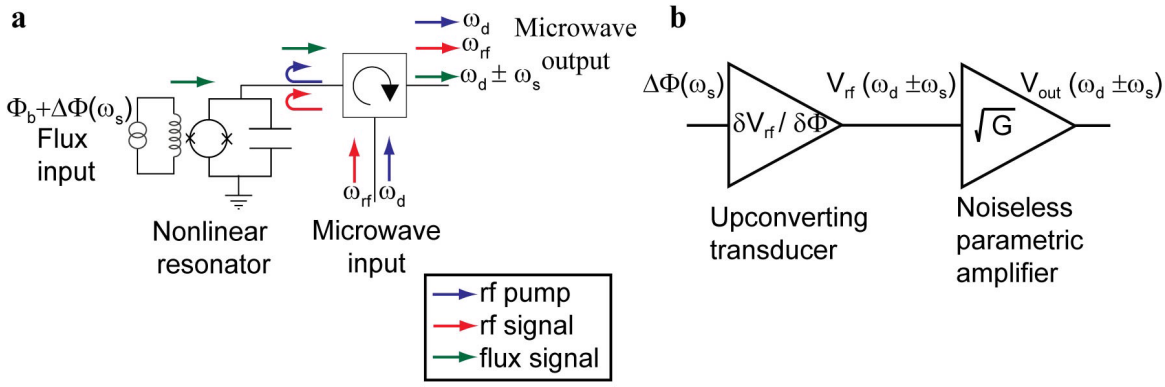

Figure 4.1: Magnetometer schematics. a) Device circuit. The magnetometer consists of the nonlinear inductance of an unshunted two-junction SQUID in parallel with an on-chip lumped-element capacitor. An applied magnetic flux (green arrows) modulates the resonant frequency, and is read out as a change in the phase of a microwave drive signal (blue arrows) reflected from the device through a circulator. If the resonator is driven strongly, any additional weak rf input signal (red arrows) will also be amplified. b) Magnetometer model. The magnetometer can be characterized as a dual stage device, the first stage being an upconverting transducer of flux to microwave voltage and the second an rf parametric amplifier.

With malice aforethought, we model the magnetometer as consisting of two stages: a transducer which upconverts a low frequency magnetic flux signal to a microwave voltage signal and a subsequent parametric gain stage (see Fig. 4.1b). Using this picture, we derive an expression for the flux sensitivity based on the circuit parameters and the parametric gain. We first consider the dynamics of the Josephson oscillator. The supercurrent $I(t)$ flowing through a tunnel junction is related to the phase difference $\delta(t)$ across it by $I(t) = I_0 \sin\delta(t)$, where I_0 is the critical current. For a SQUID with loop inductance $L \ll \Phi_0/2I_0$, the critical current of the SQUID is $I_c(\Phi) = 2I_0 \left|\cos(\frac{\pi\Phi}{\Phi_0})\right|$, where Φ_a is the flux through the SQUID loop and $\Phi_0 \equiv \hbar/2e$ is the magnetic flux quantum. Thus, we treat the SQUID as a junction with a flux dependent critical current. In our experiment the SQUID is shunted with a lumped-element capacitor, forming an electrical resonator with resonant frequency $\omega_{p0}(\Phi_a)/2\pi = \sqrt{2\pi I_c(\Phi)/(\Phi_0 C)}/2\pi$. The resonator is connected directly to a microwave transmission line of characteristic impedance Z_0 (Fig. 4.1a), resulting in a quality factor $Q = \omega_{p0} Z_0 C$.

4.3.2 Dynamic equations

The dynamics of this system are well described by the Duffing equation, in which the sinusoidal current phase relationship of the junction is truncated after the first nonlinear

term [62],

$$\frac{\partial^2\delta}{\partial t^2} + 2\Gamma\frac{\partial\delta}{\partial t} + \omega_{p0}^2(\Phi)(\delta - \frac{\delta^3}{6}) = \frac{2\pi}{\Phi_0 C} I_d \cos(\omega_d t), \tag{4.1}$$

where $\Gamma = (2Z_0C)^{-1}$, and I_d is the amplitude of the rf drive at frequency $\omega_d/2\pi$. Next we consider a flux $\Phi = \Phi_b + \Delta\Phi\cos(\omega_s t)$ applied to the SQUID, where Φ_b is a static flux bias and $\Delta\Phi \ll \Phi_0$ is the amplitude of a weak flux signal at frequency ω_s. The associated flux modulated SQUID critical current is given as $I_c(\Phi_a) = I_0\cos(\frac{\pi}{\Phi_0}[\Phi_b + \Delta\Phi\cos(\omega_s t)])$. We can expand this form, yielding

$$I_c(\Phi_a) = I_0\cos(\frac{\pi\Phi_b}{\Phi_0})\cos\left[\frac{\pi\Delta\Phi}{\Phi_0}\cos(\omega_s t)\right] + I_0\sin(\frac{\pi\Phi_b}{\Phi_0})\sin\left[\frac{\pi\Delta\Phi}{\Phi_0}\cos(\omega_s t)\right] . \tag{4.2}$$

We next use $\frac{\pi\Delta\Phi}{\Phi_0} << 1$ to expand those terms to 1st order in sine and cosine, resulting in

$$I_c(\Phi_a) = I_0\cos(\frac{\pi\Phi_b}{\Phi_0}) + I_0\sin(\frac{\pi\Phi_b}{\Phi_0})\frac{\pi\Delta\Phi}{\Phi_0}\cos(\omega_s t) \;\; = I_c(\Phi_b)\left[1 + \tan(\frac{\pi\Phi_b}{\Phi_0})\frac{\pi\Delta\Phi}{\Phi_0}\cos(\omega_s t)\right] . \tag{4.3}$$

We substitute this back into Eqn. 4.1, which yields

$$\frac{\partial^2\delta}{\partial t^2} + 2\Gamma\frac{\partial\delta}{\partial t} + \omega_{p0}^2(\Phi_b)\left[1 + \tan(\frac{\pi\Phi_b}{\Phi_0})\frac{\pi\Delta\Phi}{\Phi_0}\cos(\omega_s t)\right](\delta - \frac{\delta^3}{6}) = \frac{2\pi}{\Phi_0 C} I_d\cos(\omega_d t). \tag{4.4}$$

We calculate the system steady-state response by assuming a solution of the form $\delta(t) = \delta_0\cos(\omega_d t - \theta) + \epsilon(t)$, where the first term is the steady state solution for $\Delta\Phi = 0$ and $\epsilon(t)$ is a small perturbation of the junction phase due to $\Delta\Phi$, and substituting it into Eq. (4.4). The resulting expression for the junction phase perturbation $\epsilon(t)$ is

$$\begin{aligned} &\frac{\partial^2\epsilon}{dt^2} + 2\Gamma\frac{\partial\epsilon}{dt} + \epsilon\omega_{p0}^2\left(1 - \frac{\delta_0^2}{4}\right)\left[1 - \frac{\delta_0^2}{4 - \delta_0^2}\cos(2\omega_d t - 2\theta)\right] \\ &= \frac{\Delta\Phi}{Z_0 C\Phi_0}\frac{\partial V_{rf}}{\partial\Phi}\left[\cos(\omega_d t + \omega_s t - \theta) + \cos(\omega_d t - \omega_s t - \theta)\right]. \end{aligned} \tag{4.5}$$

4.3.3 Paramateric amplification formalism

We recognize the left hand side of Eq. 4.5 as the equation for a parametrically driven harmonic oscillator. For appropriate bias conditions, the system can amplify any additional weak rf signal with frequency $\omega_{rf}/2\pi$ near $\omega_d/2\pi$. A formalism for calculating the performance of this amplifier is developed in R. Vijay's recent Ph.D. thesis[61]. Key results from this formalism are reproduced here, and used as a guide for subsequent calculations of the sensitivity of the magnetometer.

We begin with an equation similar to Eq. 4.5, with a strong rf drive tone at frequency $\omega_d/2\pi$, and an additional weak signal tone $(\omega_d+\omega_s)/2\pi$, as shown in Fig. 4.1a as the signal tone instead of an applied flux signal, resulting in the following equation:

$$\begin{aligned}&\frac{\partial^2\epsilon}{dt^2}+2\Gamma\frac{\partial\epsilon}{dt}+\epsilon\omega_{p0}^2\left(1-\frac{\delta_0^2}{4}\right)\left[1-\frac{\delta_0^2}{4-\delta_0^2}\cos\left(2\omega_d t-2\theta\right)\right] \\ &=\frac{2\pi}{\Phi_0 C}I_{rf}\cos(\omega_d t+\omega_s t).\end{aligned} \tag{4.6}$$

We next write an equation to relate incoming and outgoing power waves (A_{in} and A_{out}) to the voltage across the parallel resonator $V(t)$:

$$A_{out}(t)=\frac{V(t)}{\sqrt{Z_0}}-A_{in}(t), \tag{4.7}$$

where outgoing power wave has associated voltage amplitude $V_{out}=A_{out}\sqrt{Z_0}$. In this notation, we re-express the right hand side of Eq. 4.6 as $\frac{4\pi}{\Phi_0 C\sqrt{Z_0}}A_{in}(t)$. We next Fourier transform the resulting equation using the convention for the Fourier transform

$$A[\omega]=\int_{-\infty}^{\infty}A(t)\,e^{i\omega t}dt,\, A(t)=\frac{1}{2\pi}\int_0^{\infty}(A[\omega]\,e^{-i\omega t}+A^{\dagger}[\omega]\,e^{i\omega t})d, \tag{4.8}$$

to yield an equation for the spectral amplitude of the SQUID oscillations $\delta_0[\omega]$, which is found to be

$$\left(\frac{\omega_p-\omega}{\Gamma}-\frac{\omega_p\varepsilon}{\Gamma}-i\right)x[\omega]-\frac{\omega_p\varepsilon}{4\Gamma}e^{2i\theta}x^{\dagger}[2\omega_d-\omega]=a_{in}[\omega]. \tag{4.9}$$

Here we have followed Vijay's conventions, with $i=\sqrt{-1}$, $\delta_0[\omega]=\sqrt{\hbar\omega/\Gamma}x[\omega]$, and $\varepsilon=\delta_0^2/4$, and made the rotating wave approximations $\omega_p+\omega\approx 2\omega_p$ and $\omega/\omega_p\approx 1$. We can further manipulate the above equation to write an equation for the spectral components of the reduced SQUID oscillations $x[\omega]$ in terms of the the frequency offset between the drive and signal tones $f=\omega_s/2\pi$, $x[\pm f]=A(\pm f)\,a_{in}[\pm f]+B(\pm f)\,a_{in}^{\dagger}[\mp f]$, with

$$\begin{aligned}A(f) &= -\frac{\Omega-2\epsilon+f+i}{\epsilon^2+(i+f)^2-(\Omega-2\epsilon)^2}, \\ B(f) &= -\frac{\epsilon e^{2i\theta}}{\epsilon^2+(i+f)^2-(\Omega-2\epsilon)^2},\end{aligned} \tag{4.10}$$

where $\Omega=(\omega_p-\omega_d)/\Gamma$ and $\rho=\omega_p\varepsilon/4\Gamma$. We can combine these three expressions with the Fourier transform of the input-output equation (Eq. 4.7) to find expressions for the signal and idler power gains of the parametric amplifier, respectively:

$$G_s=\left|\frac{a_{out}[f]}{a_{in}[f]}\right|^2=|-1-i2A(f)|^2 \tag{4.11}$$

$$G_i = \left| \frac{a_{out}\left[-f\right]}{a_{in}\left[f\right]} \right|^2 = \left|2B\left(f\right)\right|^2 . \tag{4.12}$$

Thus, we see that $A\left(f\right)$ and $B\left(f\right)$ are directly related to the the gain of the parametric amplifier, with $A\left(f\right)$ characterizing the signal gain, and $B\left(f\right)$ the idler gain. The production of both a signal and idler output from a single input is a general feature of parametric amplification. For weak drive power, these terms are small so that $G_s \approx 1$, and $G_i \approx 0$, so that the input signal reflects from the resonator with unity gain. They grow as the drive amplitude is increased and the drive frequency decreased, diverging for a critical drive conditions $\Omega \rightarrow \Omega_c = -\sqrt{3}$ and $\delta_0 \rightarrow \delta_c = \frac{4}{3^{1/4}\sqrt{Q}}$. Usefully large finite gain is achieved by approaching this bias condition from below.

A schematic of the behavior of the parametric amplifier is shown in Fig. 4.2. In this doubly degenerate mode of parametric amplification, the single sideband signal at frequency $\omega_{rf}/2\pi$ (Fig. 4.2a-b) is amplified with a voltage gain $\sqrt{G_s} \equiv \sqrt{G}$, and an idler signal is also produced at frequency $\omega_i/2\pi = (2\omega_d - \omega_{rf})/2\pi$ with gain $\sqrt{G_i} = \sqrt{G-1}$ and relative phase factor $e^{i\phi}$. In the high gain limit, the voltage signal-to-noise ratio (SNR) is degraded by a factor of at least $\sqrt{2}$, since the amplified signal is accompanied by incoherent noise from both the signal and idler frequencies. For an operating temperature $T \ll T_Q = \hbar\omega_d/2k_B$, this noise is set by the amplitude of quantum fluctuations at frequency ω_d and the amplifier is quantum limited with a noise temperature $T_N = T_Q$. Other Josephson junction based parametric amplifiers have been shown to operate with near quantum limited noise temperature [63, 64]. If such an amplifier is now presented with a double sideband signal, symmetric about the drive tone with coherent components at both the signal and idler frequencies (Fig. 4.2c), the output voltage is a coherent combination of these two signals. We can express this double sideband signal as consisting of two orthogonal quadrature signals—one which is amplified and the other deamplified. This process is shown schematically for the amplified quadrature in Fig. 4.2d. If the signal lies fully along the amplified quadrature, it is amplified without adding additional noise, a process known as phase sensitive amplification [65].

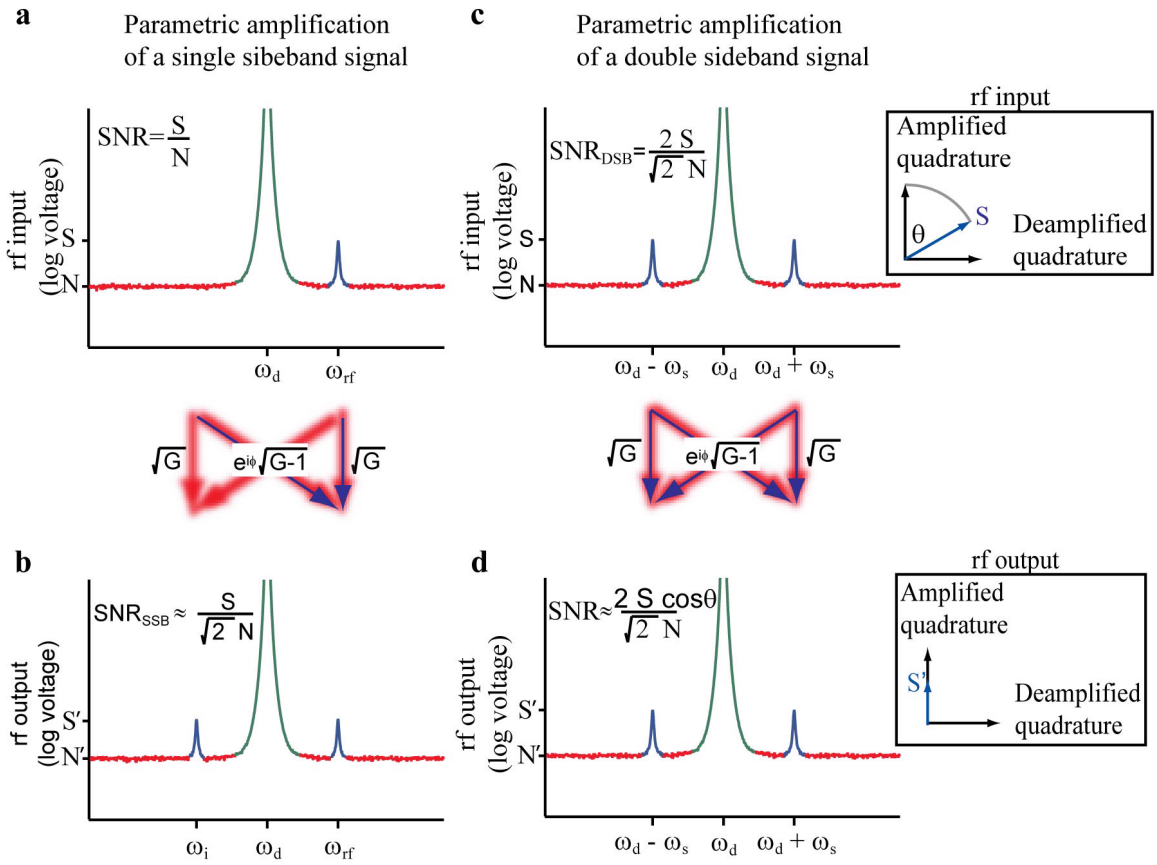

Figure 4.2: Parametric amplification. The drive tone is in green, coherent signals are in blue, and incoherent noise is in red. **a-b**. Parametric amplifier response to a single frequency rf tone. A single sideband signal at frequency $\omega_{rf}/2\pi$ (**a**) is amplified with a voltage gain $\sqrt{G}$, and an idler signal is also produced at frequency $\omega_i/2\pi = (2\omega_d - \omega_{rf})/2\pi$ with gain $\sqrt{G-1}$ and relative phase ϕ (**b**). In the high gain limit, the voltage signal-to-noise ratio (SNR) is degraded by a factor of at least $\sqrt{2}$, as the amplfied signal is accompanied by incoherent noise from both the signal and idler frequencies. **c-d.** A coherent double sideband input signal symmetric about the drive tone results in output voltages which are a coherent combination of the signal and idler tones. This process can be decomposed as amplification of two orthogonal signal quadratures—one which is amplified and the other which is deamplified. The amplitude of the output signal is determined by the magnitude of the projection of the input signal along the amplified quadrature. If the input signal lies fully along the amplified quadrature ($\theta = 0$), it will be amplified without reduction of SNR.

4.3.4 Effective flux sensitivity

Returning to our flux sensitivity calculation, we follow the same formalism as in the parametric amplifier case, focusing on parametric amplification of the transduced flux signal. Examining the right hand side of Eq. 4.5 , we see that the flux signal at frequency $\omega_s/2\pi$ has been parametrically upconverted through interaction with the drive tone, resulting in a double sideband effective rf input signal with components at frequencies $(\omega_d \pm \omega_s)/2\pi$, which can be expressed as a single quadrature signal with angle θ relative to the drive tone. The amplitude of these two signals are given by a transduction coefficient

$$\frac{\partial V_{rf}}{\partial \Phi} = \pi \frac{2 I_0 Z_0}{4\Phi_0} \sin\left(\frac{\pi \Phi_b}{\Phi_0}\right)\left(\delta_0 - \frac{\delta_0^3}{8}\right). \qquad \left(-\frac{\Phi_0}{2} < \Phi_b < \frac{\Phi_0}{2}\right) \tag{4.13}$$

Fourier transforming the right hand side of Eq. 4.5, following the conventions established in the previous section, we arrive at the result:

$$\begin{aligned} a_{in}[\omega] &= \sqrt{\frac{2}{\hbar\omega}}\frac{\sqrt{Z_0}}{2} I_0 \frac{\pi \Delta\Phi}{2\Phi_0} \sin\left(\frac{\pi\Phi_b}{\Phi_0}\right)\left(\delta_0 - \frac{\delta_0^3}{8}\right) && (4.14)\\ &\quad \left[\frac{e^{i\theta}}{2}\delta_D(\omega - (\omega_d + \omega_s)) + \frac{e^{i\theta}}{2}\delta_D(\omega - (\omega_d - \omega_s))\right] && (4.15)\\ &= a_0\left[\frac{2\pi e^{i\theta}}{2} 2\pi\delta_D(\omega - (\omega_d + \omega_s) + \frac{2\pi e^{-i\theta}}{2} 2\pi\delta_D(\omega - (\omega_d - \omega_s))\right], && (4.16)\\ \text{where } a_0 &= \sqrt{\frac{2}{\hbar\omega}}\frac{\sqrt{Z_0} I_0 \pi \Delta\Phi}{4\Phi_0} \sin\left(\frac{\pi\Phi_b}{\Phi_0}\right)\left(\delta_0 - \frac{\delta_0^3}{8}\right). && (4.17) \end{aligned}$$

We then proceed by again using considering the Fourier transform of Eq. 4.7, with the exception that there is no external applied rf signal tone in this case, only the internally generated transduced rf tones, so we write:

$$a_{out}[f] = -2ix[f]. \tag{4.18}$$

Substituting into the previous expressions for $x[f]$ in terms of $A(f)$ and $B(f)$, and focusing our attention on the upper sideband signal, we write

$$\begin{aligned} a_{out}[f] &= -2i\{A(\pm f)\, a_{in}[\pm f] + B(\pm f)\, a_{in}^{\dagger}[\mp f]\} && (4.19)\\ &= -2ia_0\{A(f)\frac{2\pi e^{i\theta}}{2} + B(f)\frac{2\pi e^{-i\theta}}{2}\}\delta_D(\omega - (\omega_d + \omega_s)). \end{aligned}$$

We can re-express this as an output voltage

$$\begin{aligned} V_{out}[f] &= A_{out}[f]\sqrt{Z_0} = \sqrt{\frac{\hbar\omega}{2}}\sqrt{Z_0}a_{out}[\omega] = \\ &\quad -2i\sqrt{\frac{\hbar\omega}{2}}\sqrt{Z_0}a_0\{A(f)\frac{2\pi e^{i\theta}}{2} + B(f)\frac{2\pi e^{-i\theta}}{2}\}\delta_D(\omega-(\omega_d+\omega_s) \\ &= -b_0 i\{A(f)\frac{e^{i\theta}}{2} + B(f)\frac{e^{-i\theta}}{2}\}\delta_D(\omega-(\omega_d+\omega_s)), \\ \text{where } b_0 &= 2\sqrt{\frac{\hbar\omega}{2}}\sqrt{Z_0}a_0 \\ &= \frac{Z_0 2I_0\pi\Delta\Phi}{4\Phi_0}\sin\left(\frac{\pi\Phi_b}{\Phi_0}\right)\left(\delta_0-\frac{\delta_0^3}{8}\right). \end{aligned} \tag{4.20}$$

Then, the magnitude of the output voltage at the upper sideband frequency $|V_{out}[f]| = b_0\left|A(f)\frac{e^{i\theta}}{2} + B(f)\frac{e^{-i\theta}}{2}\right|$. In the high gain limit, we can write the combination of upper and lower sideband information, represented in the above equation as a combination of complex A and B coefficients, as a total voltage gain of $2\sqrt{G}\cos(\theta)$, with the final result

$$|V_{out}[f]| = \Delta\Phi\frac{\partial V_{rf}}{\partial\Phi}\left[2\sqrt{G}\cos\theta\right] = \Delta\Phi\frac{\partial V_{rf}}{\partial\Phi}\eta\sqrt{G}. \tag{4.21}$$

At finite gain, the angles between $A(f)$ and $B(f)$ and the transduced signal are a complicated function of the bias parameters, and the signal and idler gain are not equal. We encapsulate these considerations in the factor η, which can summarizes the consequences of the phase sensitive nature of the parametric amplification. In the high gain limit, the component of the transduced signal which lies along the amplified quadrature of the phase sensitive amplifier is noiselessly amplified with gain $\sqrt{G}$, and η can expressed simply as $\eta = 2\cos\theta$. The transduced signal, however, does not lie fully along the amplified quadrature at high gain points ($\theta \neq 0$), so that the total gain is reduced. As $G \to \infty$, this angle, which represents the angle between the external drive and the internal oscillation, is given by $\theta \to 60°$, so that the total gain is given by $\eta = 2\sqrt{G}\cos\theta \approx \sqrt{G}$.

4.3.5 Effective Flux Noise

To characterize the flux sensitivity of the magnetometer, we refer the noise of the output rf voltage signal to an effective input flux noise via the total transduction coefficient $\eta\frac{\partial V_{rf}}{\partial\Phi}$. This effective flux noise has a spectral density

$$S^{1/2}_{\Phi eff}(\Phi_0/\sqrt{Hz}) = \frac{\sqrt{2(k_B T_{sys}+\hbar\omega_d/2)Z_0}}{\eta\frac{\partial V_{rf}}{\partial\Phi}\Phi_0} = \frac{4}{\pi}\frac{\sqrt{2(k_B T_{sys}+\hbar\omega_d/2)Z_0}}{2I_0 Z_0\eta\sin\left(\frac{\pi\Phi_b}{\Phi_0}\right)\left(\delta_0-\frac{\delta_0^3}{8}\right)}, \tag{4.22}$$

where T_{sys} is the system noise temperature.

For weak drive amplitudes, where the resonator response is linear and $G = 1$, T_{sys} is determined by the cryogenic high electron mobility transistor (HEMT) semiconductor amplifier (see Fig. 5.2), whose noise temperature T_{HEMT} is much larger than the quantum

limit. Furthermore, we can express the junction oscillation amplitude in terms of the voltage drive as $\delta_0 - \frac{\delta_0^3}{8} \approx \delta_0 \approx \frac{V_d Q}{Z_0 2 I_0}$. In the absence of parametric amplification, we can also set $\eta = 1$ to yield

$$S_{\Phi eff}^{1/2}(\Phi_0/\sqrt{Hz}) \approx \frac{4}{\pi} \frac{\sqrt{2 k_B T_{HEMT} Z_0}}{\sin\left(\frac{\pi \Phi_b}{\Phi_0}\right) V_d Q} \text{ for } G = 1, \tag{4.23}$$

which varies inversely with resonator Q and drive voltage V_d. Thus, in this regime higher sensitivity can be achieved by increasing the Q of the resonator and the drive amplitude. In practice, however, the maximum drive voltage is limited by the onset of nonlinearity inherent in any SQUID based resonator [66].

For strong drive amplitudes, where the resonator response is nonlinear and $G \gg 1$, the noise temperature of the system is determined by the amplitude of quantum fluctuations at the drive frequency. Thus, the system noise temperature is given by $T_{sys} \approx \hbar \omega_d / 2 k_B$. Further, as $G \to \infty$, δ_0 approaches a critical value of $\delta_c = \frac{4}{3^{1/4}\sqrt{Q}}$[66]. For $Q \gtrsim 10$, $\delta_c \leq 1$ and we can make the approximation $\delta_0 - \frac{\delta_0^3}{8} \approx \delta_c$. Similarly, the angle θ also approaches a critical value of 60°, so that we can approximate $\eta \approx 1$ to yield

$$S_{\Phi eff}^{1/2}(\Phi_0/\sqrt{Hz}) \approx \frac{(2\sqrt{3})^{1/2}}{\pi} \frac{\sqrt{\hbar \omega_d}}{2 I_0 \sin\left(\frac{\pi \Phi_b}{\Phi_0}\right)} \sqrt{\frac{Q}{Z_0}} \text{ for } G \gg 1. \tag{4.24}$$

This expression has the remarkable feature that the effective flux noise varies directly with the resonator Q, so that a resonator with lower Q has improved flux sensitivity. This results from the requirements of parametric amplification, in particular that high parametric gain occurs at a critical phase oscillation $\delta_c \propto Q^{-1/2}$, which in turn limits the maximum achievable transduction coefficient. Additionally, lowering the resonator Q leads to parametric amplification with increased bandwidth for a given parametric gain, and so is doubly desirable. In both the linear and nonlinear regime, it is advantageous to increase the SQUID critical current and operate at a flux bias near $\Phi_0/2$.

Chapter 5

Tunnel junction dispersive magnetometer prototype

In this chapter we present measurements conducted on Al-AlO_x-Al tunnel-junction based dispersive magnetometers. These devices can also be used in the measurement of submicron-scale magnetic samples in fields up to a few hundred millitesla. Measurements on these samples will allow development of the rest of the measurement system while work on development of fabrication techniques to reproducibly manufacture well characterized aluminum nanobridges is in progress.

5.1 Sample design and fabrication

As detailed in Eq. 4.24, maximum sensitivity is achieved in our dispersive magnetometer by minimizing the resonator quality factor Q. It is also necessary to avoid excess geometric inductance, which effectively dilutes the effect of the nonlinear SQUID inductance. Both of these conditions can be readily satisfied in a lumped element parallel-resonator geometry (shown in Fig. 5.1). The resonator is connected directly to the microwave environment, so that the microwave impedance directly shunts the resonator, forming a parallel LCR resonator with $R = Z_0$, where Z_0 is the characteristic microwave impedance. In the case of our differential excitation geometry, this impedance is twice the usual value, $Z_0 = 100\ \Omega$, due to the microwave hybrid launch (detailed in Sec. 5.2.3). The device consists of three layers: a 250-nm thick Nb underlayer, a 180-nm thick SiN_x insulating layer, and an aluminum upper layer. The capacitor was fabricated in a split geometry, with both electrodes on the top Al layer connected through the Nb underlayer. The SQUID was fabricated with double-angle evaporated Al-AlO_x-Al junctions. A short-circuit terminated coplanar waveguide transmission line was also fabricated on chip to allow us to apply oscillating flux signals to the SQUID loop. The sample base of Nb ground planes covered with SiN_x were fabricated by Jed Johnson and Daniel Slichter. The aluminum top layer was fabricated by R. Vijay. These devices are designated by their design number, NS006, and serial number within that series. The measurements presented in the remainder of this chapter are of devices NS006.05 and NS006.06.

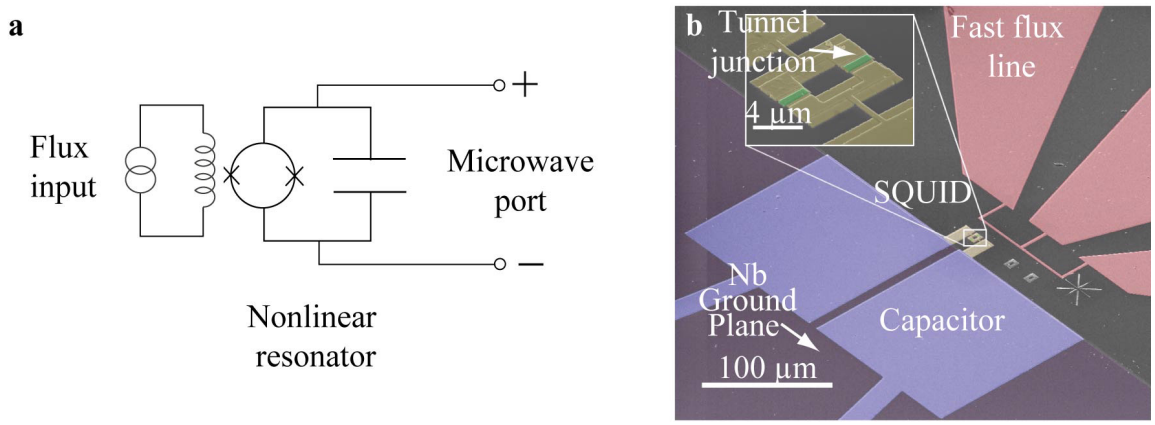

Figure 5.1: Schematic and image of tunnel junction prototype. **a.** Schematic of magnetometer, showing flux port and differential microwave port. **b.** False color scanning electron microscope image of the dispersive magnetometer. The SQUID is shown magnified in the inset, with the Al-AlO_x-Al tunnel junctions marked in green. The capacitor is formed in a split geometry, with two top layer electrodes connected through a common niobium plane. A high bandwidth flux line is formed by a short circuit terminated coplanar waveguide transmission line, shown in the upper right of the figure.

5.2 Microwave and cryogenic configuration

5.2.1 Cryogenic setup

The samples were cooled and measured on the 4-8 GHz channel of the cryogen-free Vericold dilution refrigerator (DR) in the Quantum Nanoelectronics Lab (QNL). In order to accommodate a number of potential experiments with these samples, they were mounted in a somewhat complicated back-to-back configuration, as detailed in Fig. 5.2. In this setup sample 1 can be driven through rf input #1, and the output reflects from sample 2 before continuing to the output amplification chain. If sample 2 is flux biased to a much different resonant frequency, the sample reflects with unity gain. If the samples are flux biased to similar resonant frequencies, the two devices can be used as cascaded parametric amplifiers, as a flux transducer followed by a parametric amplifier, or some combination of the two. RF input line #2 allows the drive tone reflected from sample 1 to be cancelled or modified prior to reaching sample 2, allowing the two resonators to be driven with distinct drive amplitudes, phases, and frequencies.

Both input lines are heavily attenuated (with XMA 2782-6051-10 and -20 attenuators) to avoid coupling thermal fluctuations from higher temperature stages into the resonators which degrade their performance. RF input #2 has 20 dB less fixed attenuation to compensate for the -20 dB coupling through the directional coupler (Krytar 102008020) at the end of the line. High-pass and low-pass filters (Minicircuits VHF-3800 and VLF-7200) are used in both input lines to additionally attenuate input signals outside the 4-8

GHz bandwidth of the cryogenic circulator and isolators (PAMTECH CTH1368K18) are used both to couple the samples and to provide reverse isolation in the output line. The output signal is amplified at the second pulse-tube stage with a low noise temperature HEMT amplifier (Cal-Tech CITCRYO 1-12A); the temperature of the stage in these experiments was around 5.5 K. Additional amplification occurs at room temperature (using Miteq AF3 and/or AFS4 amplifiers), depending on the application. Inner/outer conductor dc blocks (INMET 803) are used to isolate the potentially noisy instrument grounds from the DR ground, which is provided through a direct large gauge copper grounding cable tied to an isolated ground rod a few meters away. The flux line is similarly constructed, with flat phase delay 120 MHz low pass filters (Minicircuits SBLP-200) and in-house fabricated matched lossy transmission line filters[67], which prevent re-entry at higher frequencies. The single injection line is switched between three possible outputs through the use of a latching, mechanical dc-18 GHz 1-3 way switch at base temperature (Radiall R573423300), which has been modified in-house to function at cryogenic temperatures.

All components have been carefully selected to perform at cryogenic temperatures. The rf coaxial cable materials are chosen to bridge the DR temperature stages without thermal loading. On the injection lines and after the HEMT amplifier on the output line, where losses are not a concern, stainless steel inner and outer conductor 2.159 mm (0.085") diameter coaxial cable (Micro-coax UT-85-SS-SS) is used. The losses of these cables, which are specified at 4.66 dB/m at 5 GHz and 300 K, are not expected to change appreciably with temperature, and contribute an additional $\sim$10 dB of loss to the fixed attenuation of the injection lines. Connections between elements at the same temperature are made with tin-plated copper coaxial cable (UT-85-TP-M17), and the return line from the base-temperature stage to the HEMT amplifier is constructed of silver-flashed CuNi inner/CuNi outer coaxial cable (coax.co.jp SS-219/50-SCN-CN), which has excellent thermal isolation and lower losses than the stainless steel coaxial cable. High performance 3.5 mm connectors (SGMC 200-37-20-850 (female) and 200-36-20-850 (male)) connectors are used for all permanent DR wiring, and SMA connectors (Radiall 9401-1583-010) are used for other connections.

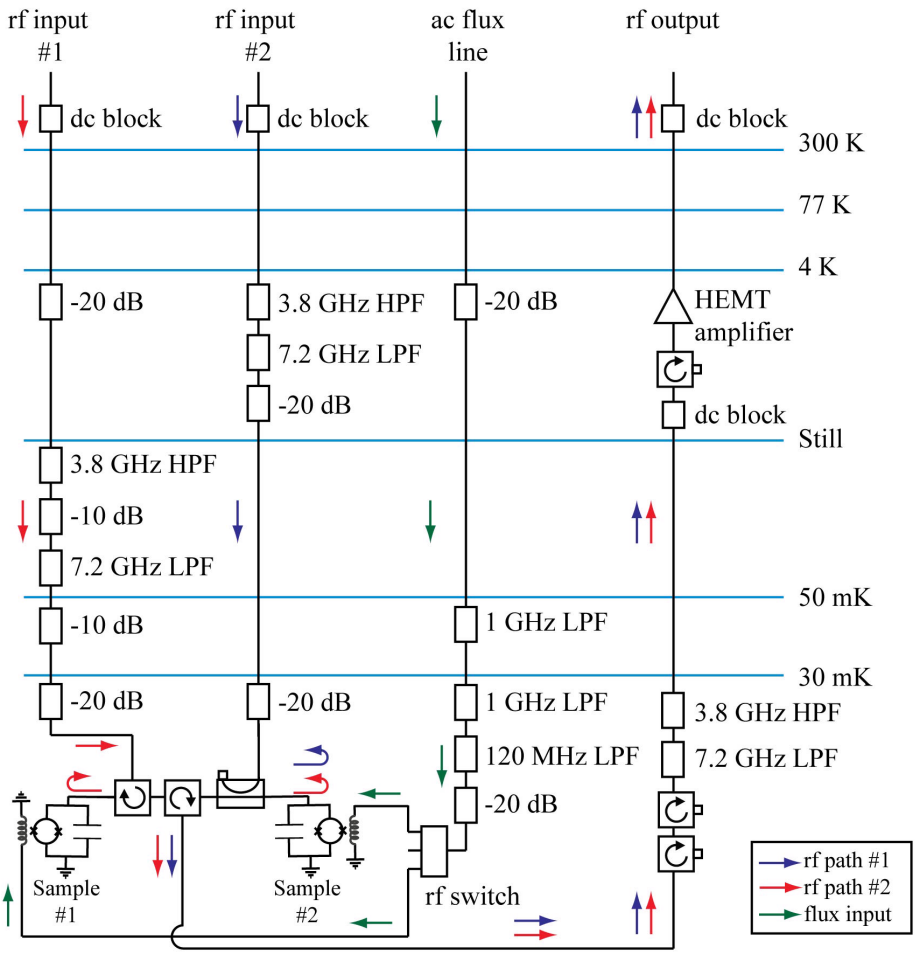

Figure 5.2: Rf configuration of dilution refrigerator. The dilution refrigerator stages are shown in light blue. The two samples are arranged so that they can be excited either separately, or cascaded in series with the pair of rf input lines (red and blue arrows), and fed into a common output line. AC flux signals are applied to either sample one or two through a single flux input line which passes through a 3-way rf switch. Superconducting magnet coils for dc flux bias of each sample are not shown.

5.2.2 Longitudinal and transverse magnets

In order to provide the longitudinal and transverse fields required to manipulate electron spins and the provide SQUID bias flux, a two-axis magnet rig (shown in Fig. 5.3) was designed and constructed. The magnets are wound using NbTi superconducting wires in a CuNi matrix (Supercon 15S40-0.0055") on copper coil frames. The CuNi matrix allows the leads from the magnets to be run to higher temperature stages without thermally loading the base stage on which they are mounted. The longitudinal magnet was designed

with the minimum bore size which would accommodate the rf launch (detailed in the next section). Following the magnet design rules detailed in Chapter 3, the SQUID and sample are suspended in the center of the solenoid bore to achieve maximum field strength and homogeneity. The transverse coil, which is only required to provide a field on the order of a flux quantum through the SQUID washer, was wound to be as small as possible in order to fit in the bore of the longitudinal magnet, and is mounted with its bore directly beneath the SQUID washer. In order to cool the sample in as low a magnetic field as possible and shield against magnetic noise, the entire magnet assembly is mounted in a combination Cryoperm and aluminum superconducting shield. The Cryoperm shield serves to minimize the field density in the aluminum shield as it cools through its critical temperature, after which the field in the aluminum shield is frozen in and subsequent changes shielded by the superconductor. The aluminum shield is constructed of 6061 alloy aluminum with a press-fitted bottom piece mounted to a square, hollow tube and a bolt-on top piece with high aspect-ratio penetrations for dc and rf cabling and long overlap with the square, hollow tube to minimize field penetrations. Thermalization of the magnet assembly is accomplished through 2.159 mm (0.085") copper cables which pass through the shield top piece. The assembly shown in the figure is currently mounted on a helium-3 refrigerator. The large longitudinal magnet, which requires high current (several ampere) carrying lines that are not currently installed on the DR, has been omitted in the otherwise similar magnet rig used for the measurements presented in later sections of this chapter. Additionally, the lines feeding the transverse coil in the DR are heavily filtered with multiple stages of LC π-filters and copper powder filters to minimize magnetic noise coupled through the magnet.

5.2.3 Microwave launch

The sample is driven with a modified 180° hybrid, which converts the single ended 50 Ω characteristic impedance microwave signal to a 100 Ω differential signal. The hybrid is based on the classic ratrace hybrid design [52], fabricated in a microstrip geometry on 1/2 oz. copper-clad 0.635 mm Rogers 3006 microwave substrate. The signal is applied to the hybrid Δ-port, and the output is applied to the sample after a microstrip to coplanar microstripline transition, as shown in Fig. 5.4. The Σ-port is un-needed, and would require either another microwave port or an on-chip termination. It has been omitted, and the impedance of the odd mode compensated by adjusting the impedance of the ring. It was found through simulations using Microwave Office that replacing the $Z_0 = 70.7\ \Omega$ $\pi/4$-wavelength segments with 25 Ω segments improves the phase and amplitude imbalance of the odd mode.

Directly connecting the hybrid to the sample has several benefits. Phase imbalance issues are minimized by the short distance between the hybrid, and the arms are lithographically determined, improving the balance. It also minimizes the size of the close loop formed by the hybrid and sample, minimizing magnetic pick up. The fractional bandwidth of the basic hybrid (approximately 0.35 of the band center frequency), though much less than those of more complicated commercial hybrids, is similar to that of the 4-8 GHz isolators in use in the output line.

The fast flux line is connected to a tapered segment of CPW line, launched with a Rosenberger solder mount connector (Rosenberger 195102-40ML solder mount connector

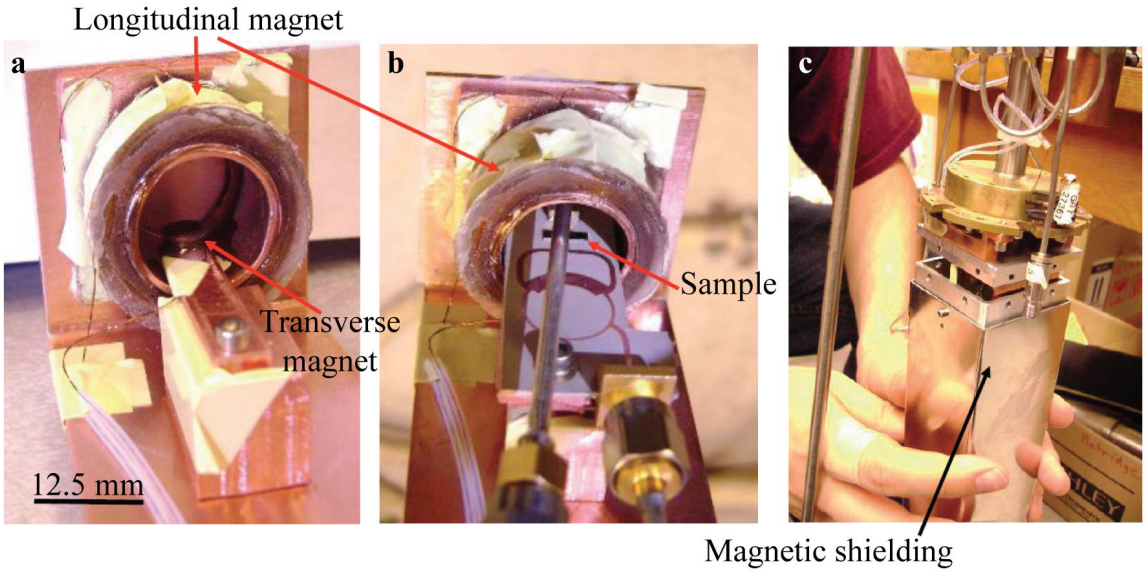

Figure 5.3: Images of magnets and magnetic shielding. **a.** The smaller transverse magnet for biasing the SQUID and larger coil for tesla scale fields in the plane of the SQUID washer. **b.** The microwave launch and sample mounted in the bore of the longitudinal magnet (transverse magnet fits into a cavity in the launch). **c.** The magnets and sample are mounted in a cryoperm and aluminum superconducting shield.

and 19K202-271L5 cable connector) on a separate Rogers board. Both boards are soldered to a copper frame for structural strength. The frame includes a 0.381 mm thick copper bridge above a pocket for the transverse magnet, which mounts the chip flush with the upper surface of the microwave substrate, minimizing bond lengths. The signal is launched onto the hybrid board with a Gigalane PSF-S01-006 SMA connector.

5.3 Measurements

5.3.1 Readout method and basic characterization

To determine the dependence of resonant frequency on applied flux, we used a vector network analyzer to measure the phase of a weak microwave tone reflected from the resonator as a function of frequency and flux. The results for sample #1 (NS006.05) are shown in Fig. 5.5. As the flux through the SQUID washer was varied, the resonant frequency was tuned from a maximum of 7.2 GHz to a minimum of 4 GHz, set by the low frequency cutoff of the circulators used in the measurement chain. The applied microwave power is -143 dBm at the plane of the magnetometer, low enough to ensure that the resonator is linear for all values of applied flux. The horizontal bands apparent in the plot are due to the finite directivity of the circulator used to separate the incoming and outgoing microwave signals from the resonator. Data from sample #2 (NS006.06) were qualitatively

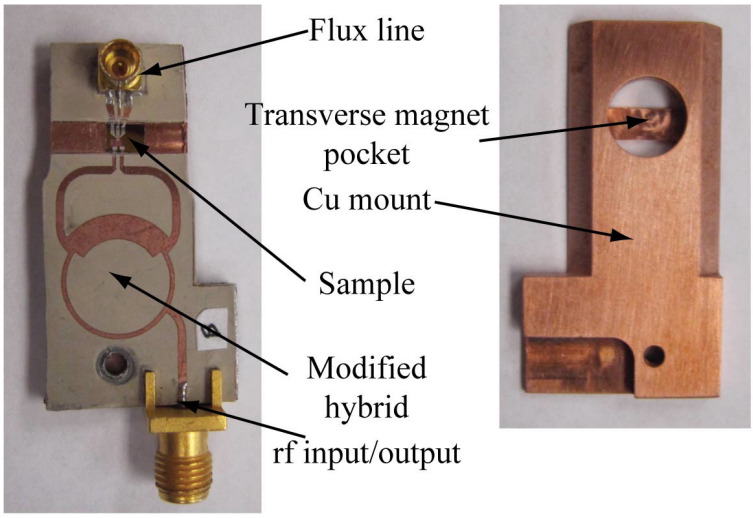

Figure 5.4: Images of rf launch. The launch consists of a copper mount to which are soldered two Rogers 3006 boards containing the flux line and rf port microwave launches. The sample is glued directly to the copper mount and electrically connected with aluminum wire bonds.

similar, with a slightly higher maximum resonant frequency. The data were fit to extract the relative values of the SQUID inductance vs. flux and stray inductance in series with the SQUID. These were converted to absolute inductances by assuming that capacitance C=4.1 pF (a value determined from examination of previous NS006 samples), yielding $L_{stray} = 50$ pH (in agreement with previous NS006 samples) and $2I_0 = 4.3$ μA. The quality factor was estimated through fits of the parametric gain versus detuning frequency to be $Q = 26$ for $\omega_0/2\pi = 5.8$ GHz.

We next experimented with a variety of bias conditions for the two samples, both separately and in series. We discovered several important features of these devices. First, we were unable to operate the devices successfully as cascaded parametric amplifiers. The two devices together did not exceed the gain possible with one device alone. Subsequent numerical simulations of individual parametric amplifier performance have indicated that the device is saturated by quantum fluctuations even at low gain values due to its broad bandwidth. This effect is still under investigation.

Further, we found that it was extremely difficult to achieve stable operation of a multi-stage device due to phase and amplitude instabilities in the drive tones. Successful operation in the nonlinear regime of either sample requires 0.01 dB level stability of the drive tone biasing that sample. In multiple stage devices, providing suitable drive amplitudes and phases to both samples at the same time requires amplitude stability and sub-degree phase stability of a combination of drive tones and cancellation tones which simultaneously satisfy the bias requirements of each sample. We attempted to address phase stability issues by sourcing the drive and/or cancellation tones from a single generator, and using variable

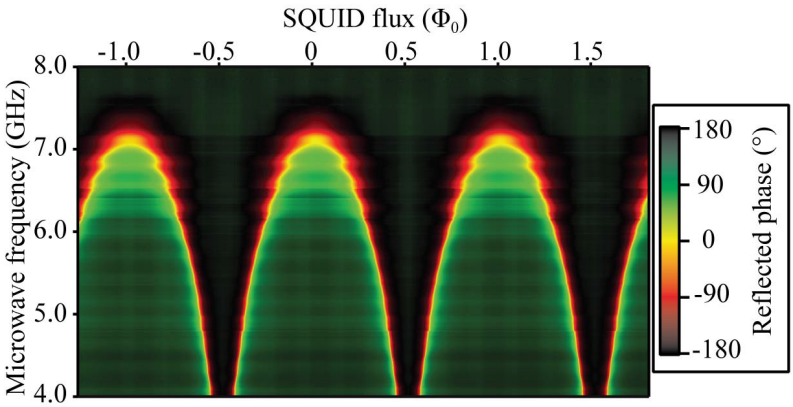

Figure 5.5: Resonator response to static flux. The phase of the reflected microwave drive is plotted versus applied SQUID flux and drive frequency. The periodicity of the SQUID inductance versus flux is evident in the pattern of reflected phase.

attenuators and phase shifters to adjust the relative amplitudes and phases. However, the amplitude stability was particularly effected by the use of these components, resulting in strong temperature dependence of device performance (including air conditioner and day-night cycles) and preventing accurate measurements. Consequently, multi-stage data are not presented here.

All subsequent measurements were conducted on sample #1, with the configuration shown in Fig. 5.6. This configuration involved a minimum of room temperature components, using separate generators to produce tones with variable amplitude and phase, connected to the fridge with minimum cable length. All instruments were frequency locked using a SRS FS725 ovenized Rb frequency standard. The rf drive tone for parametric amplifier and magnetometer measurements was provided with the E8267C generator. A separate drive cancellation tone was provided by the E8257C generator, and applied to cancel the drive tone before the output signal passes through the HEMT amplifier, reducing 1/f noise issues and drive tone contamination in the output signal. A weak rf probe tone for measuring parametric gain was provided by the Vector Network Analyzer (VNA). The VNA was operated in arbitrary sweep mode to logarithmically sweep a series of offset frequencies, allowing parametric gain curves similar to those shown in Fig. 5.7 to be generated in real time by measuring the forward transmission parameter S_{21} with the drive tone on vs. off. This capability was used to determine the maximum gain at low offset frequencies for a given drive frequency by varying the drive power while monitoring the parametric gain. All bias points displayed in Figs 5.7-5.9 were established in this way. Once a bias point was established, the VNA was switched to CWT mode to source a fixed frequency tone, and rf gain and flux response were measured simultaneously by applying a drive tone, rf probe tone, and flux signal tone simultaneously. The demodulated output signal was recorded using the I/Q demodulator, IF amplifier/filter and Acquiris DP240 digitizer. The IF amplifiers were TI OPA-420 op-amps on TI DEM-OPA-SO demonstration boards, with

filtering provided by SRS SR560 preamplifier/filter units. The sample was flux biased at $\Phi_b = 0.3\Phi_0$, where the flux sensitivity was high and the frequency band was clear of ripples which could obscure the response to rf and magnetic signals.

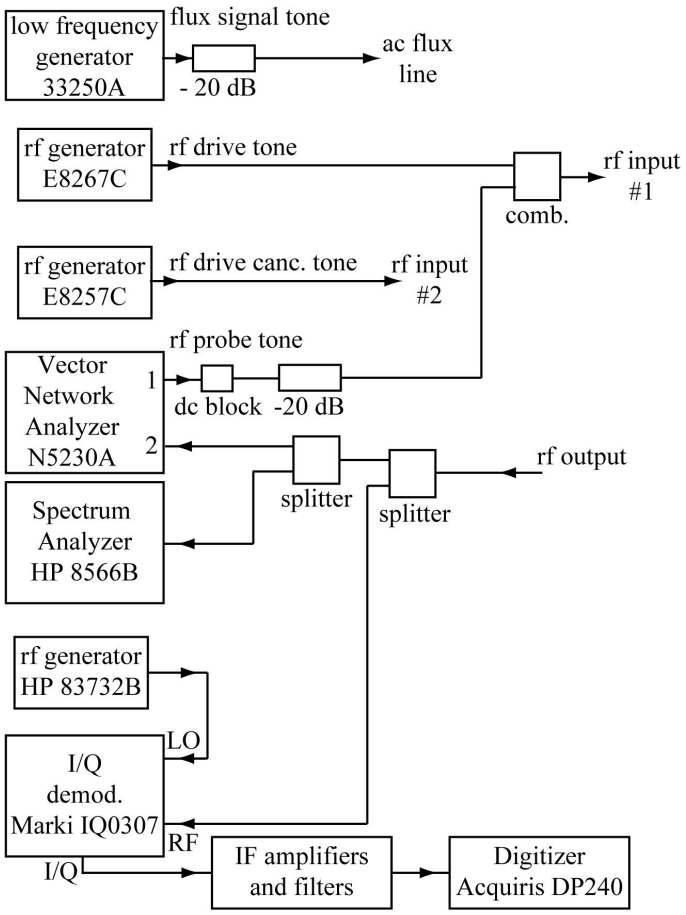

Figure 5.6: Diagram of measurement configuration. This configuration allows simultaneous measurements of both parametric gain and flux response. Stability was maximized through minimum use of room temperature components and short coaxial cables.

5.3.2 Parametric amplifier characterization

To characterize the performance of our magnetometer/parametric amplifier prototype, we first measured the parametric gain. To characterize the gain, a strong rf drive tone at frequency $\omega_d/2\pi$ was applied to the resonator simultaneously with a weak rf signal at frequency $\omega_{rf}/2\pi$ (as shown schematically in Fig. 4.2). The reflected rf signal was further amplified, demodulated by a double sideband mixer with local oscillator frequency $\omega_{LO}/2\pi = \omega_{rf}/2\pi + 110$ Hz, and digitized. The gain was measured by comparing the ratio of the reflected microwave signal with the drive tone on and off. The gain is plotted in

Fig. 5.7 as a function of the frequency offset $(\omega_{rf} - \omega_d)/2\pi$ for different drive powers. The advantage of low resonator Q is evident in these data, where a gain of 15 dB is demonstrated with a -3 dB full-bandwidth of 40 MHz. Note that the observed gain and bandwidth deviate slightly from the analytical solution of the simple Duffing oscillator prediction for a given drive amplitude. This discrepancy is resolved using numerical simulations which indicate gain suppression due to noise rounding in nonlinear resonators with very low Q.

In separate measurements using a hot/cold load, we found the system noise temperature from the plane of the parametric amplifier. The hot load source was a 50 Ω termination (XMA 2003-8810-00), anchored at 5.6 K, and connected to the base stage with a CuNi coaxial cable. A similar termination anchored at base temperature was used as the cold source, and the noise was coupled to the plane of the amplifier using a Hittite 107821-1 semiconductor switch, which enabled the two noise sources to be chopped at 111 Hz, producing a square wave signal in the system output noise. The system output noise was fed into the spectrum analyzer in zero-span mode, the resultant power level was then fed into an SRS lock-in detector, and the amplitude of the square wave signal was used to determine the total system noise temperature. The system noise temperature was found to be between 29 and 37.5 K, with the scatter arising from the uncertainty in the attenuation of the CuNi cable and semiconductor switch. This value is rather high, due to the high noise temperature of our HEMT amplifier (approximately 8 K), and large losses (approximately 6 dB, due to losses in the CuNi coaxial cable and insertion losses in the many stages of circulators and isolators) between the resonator plane and the HEMT.

By measuring the SNR improvement of rf signals measured with drive tone off versus on, we can calculate T_{sys} as a function of drive tone power, as shown in Fig. 5.7b. The uncertainty in the calculated T_{sys} is due the previously mentioned uncertainty in T_{sys} for $G = 0$. For the bias with gain $G = 32$ dB at $\omega_d/2\pi = 5.56\,\mathrm{GHz}$, we calculate T_{sys} to be between 0.14 and 0.21 K, corresponding to an added noise of 0.50 to 0.78 photons. At the highest gain point, the noise temperature was degraded due to instabilities associated with operation near the critical point [68].

5.3.3 Magnetometer characterization

The flux response of the system was simultaneously investigated by applying a flux tone at frequency $\omega_s/2\pi$, chosen so that the upper sideband of the upconverted rf output at frequency $(\omega_d + \omega_s)/2\pi$ was 10 Hz offset from the applied rf signal at frequency $\omega_{rf}/2\pi$. This allows simultaneous measurements of the parametric gain and flux sensitivity. The output signals were again amplified, demodulated with a double sideband mixer with local oscillator frequency $\omega_{LO}/2\pi = \omega_{rf}/2\pi + 110$ Hz, and digitized. The SNR of the flux response at each bias point was calculated by comparing the height of the transduced output signal to the average of the white noise in a bandwidth of 200 Hz. This SNR was converted into an effective flux noise using the known amplitude of the flux signal applied to the magnetometer. In Fig. 5.8, the effective flux noise is plotted as a function of drive amplitude and flux signal frequency. In the linear regime, the magnetometer bandwidth exceeds that of our flux excitation line, but is demonstrated to be at least 80 MHz and is consistent with our resonator Q. By biasing the resonator in the nonlinear regime, we trade bandwidth for parametric gain and reduced noise. By operating at a parametric gain

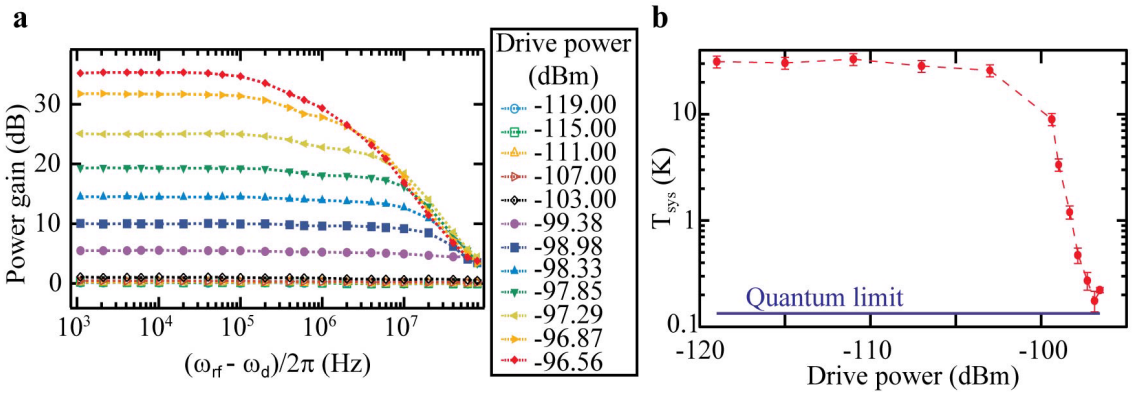

Figure 5.7: Device parametric gain and system noise temperature. **a.** The parametric gain of rf signals applied in combination with an rf drive tone versus the offset frequency $(\omega_{rf} - \omega_d)/2\pi$. Each curve is identified by the applied microwave power of the drive tone at the plane of the resonator. For low drive powers (< -103 dBm) the resonator response is linear, and consequently the parametric gain is 0 dB. At higher drive powers, the drive power was chosen so that maximum gain was achieved at a given drive frequency, as the drive frequency was decreased from 5.778 GHz at parametric gain of 0 dB to 5.556 GHz at 35 dB gain. **b.** System noise temperature (K) vs. drive power (dBm). The error bars are due to uncertainty in system noise temperature in the absence of parametric gain. The standard quantum limit ($T_{sys} = 0.14$ K at $\omega/2\pi = 5.56$ GHz) is shown in blue. At 32 dB gain the device is nearly quantum limited.

of 32 dB, we achieved a minimum effective flux noise of 0.21 $\mu\Phi_0\text{Hz}^{-\frac{1}{2}}$ at $\omega_s/2\pi = 100$ kHz. However, this is not the lowest attainable noise as the demodulated noise in these measurements with $\omega_{LO} \neq \omega_d$ is the sum of incoherent noise sidebands above and below the LO frequency, thus degrading the effective flux noise.

5.3.4 Ultimate flux sensitivity

To determine the optimum device performance, we performed a second set of measurements with $\omega_{LO} = \omega_d$. With this demodulation technique use was made of the single quadrature nature of the transduced flux signal. The effective flux noise as function of drive power measured at $\omega_s/2\pi$ =100 kHz for both demodulation techniques is shown in Fig. 5.9 and clearly demonstrates the advantage of demodulating with $\omega_{LO} = \omega_d$. The data are in good agreement with the expected noise improvement factor of 2 for $G = 1$, and $\sqrt{2}$ for $G >> 1$. The minimum effective flux noise of 0.14 $\mu\Phi_0\text{Hz}^{-\frac{1}{2}}$ was achieved with $G = 32$ dB, with a flux signal bandwidth of 600 kHz set by the parametric amplifier half bandwidth. If the system parameters are substituted into in Eq. 4.24, it predicts a minimum effective flux noise of 0.14 ± 0.007 $\mu\Phi_0\text{Hz}^{-\frac{1}{2}}$, in very good quantitative agreement with our measured results. As a final note, I observe that by reducing the parametric gain to 15 dB, an effective flux noise of 0.29 $\mu\Phi_0\text{Hz}^{-\frac{1}{2}}$ was achieved while significantly increasing

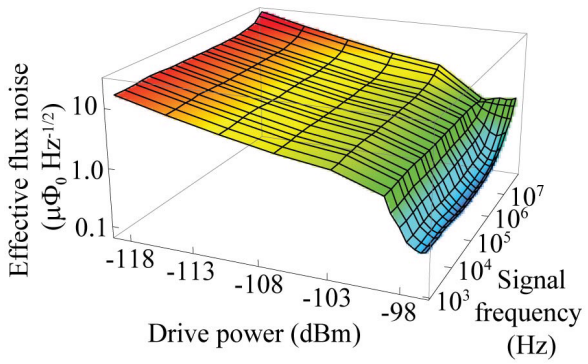

Figure 5.8: Effective flux noise. Effective flux noise versus microwave drive power at the resonator in dBm and flux signal frequency $\omega_s/2\pi$ in Hz. For drive powers below -103 dBm, the bandwidth of the flux response is set by the Q of the resonator, and is greater than 80 MHz. At higher bias powers, parametric amplification occurs, decreasing the effective flux noise until the noise of the system is set by quantum fluctuations. To avoid phase sensitive recombination of signal and idler tones in the simultaneously measured rf signal, these data were demodulated at frequency $\omega_{LO}/2\pi = (\omega_d + \omega_s)/2\pi + 110$ Hz. This degraded the flux response of the system by mixing incoherent noise from signal bands above and below ω_{LO} into the digitized signal.

the flux signal bandwidth to 20 MHz.

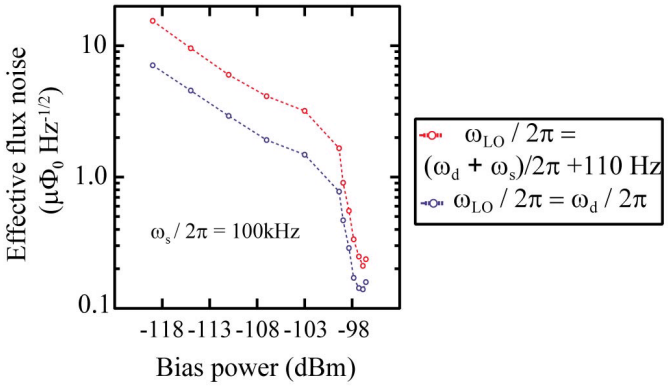

Figure 5.9: Flux Sensitivity for two demodulation frequencies. Data from Fig. 5.8 with $\omega_s/2\pi$ =100 kHz, shown in red, and are compared with flux signals at the same flux signal and bias powers demodulated at $\omega_{LO} = \omega_d$, shown in blue. In this scheme the phase of the LO signal relative to the drive signal at the mixer determines whether the upper and lower sidebands will be combined constructively or destructively. At each bias point, the phase of the LO signal was varied to achieve maximum sensitivity. In the linear regime, the latter demodulation scheme has one-half the effective flux noise, by recombining both sidebands versus mixing together one sideband with a frequency containing only noise. At high drive powers the improvement is $\sqrt{2}$, as the single output sideband contains all flux information and the $\omega_{LO} = \omega_d$ demodulation scheme still avoids mixing excess noise from an empty sideband into the digitized signal.

5.4 Future work

We have demonstrated a dispersive magnetometer based on a lumped-element, nonlinear resonator involving a two-junction SQUID. When the rf drive is sufficiently strong to achieve a high degree of nonlinearity, but is below the threshold for bifurcation, depending on the operating conditions we have achieved a gain as high as 35 dB, an effective flux noise as low as 0.14 $\mu\Phi_0\text{Hz}^{-\frac{1}{2}}$ and a bandwidth as large as 20 MHz. We expect that our magnetometer will exhibit low backaction, since the SQUID never switches to the voltage state, making it attractive for quantum state measurement. There are several avenues for further improvement. The magnetometer can be realized as two physically separate devices, a transducer and a gain stage, provided the stability issues can be addressed. This would allow for independent optimization of the transduction coefficient and the performance of the parametric amplifier. By increasing the Q of the transduction stage to match the bandwidth of the parametric amplifier, and rotating the transduced signal fully into the amplified quadrature, reductions of about 10 in the effective flux noise should be possible. A lower effective flux noise could also be achieved by optimizing the transduction coefficient

using junctions with higher critical currents, and by operating at a flux bias closer to $\Phi_0/2$. An increased bandwidth could be obtained by reducing the noise temperature of the microwave postamplifier, thus reducing the parametric gain necessary for quantum noise limited operation. Moreover, the quantum noise limited amplification we have observed suggests that this device can be used as a general purpose first-stage rf amplifier for a variety of applications. Finally, the inclusion of nanobridge junctions will allow us to characterize nanoscale magnets, as well as measure micron scale magnetism at lower magnetic fields with our existing tunnel junction design. Such measurements are currently underway at QNL.

Bibliography

[1] C.H. van der Wal, A.C.J. ter Haar, F.K. Wilhelm, R.N. Schouten, C.J.P.M. Harmans, T.P. Orlando, S. Lloyd, and J.E. Mooij. Quantum superposition of macroscopic persistent-current states. *Science*, 290:773, 2000.

[2] S. D. Bader. Colloquium: Opportunities in nanomagnetism. *Rev. Mod. Phys.*, 78(1), 2006.

[3] W Wernsdorfer. From micro- to nano-SQUIDs: applications to nanomagnetism. *Sup. Sci. Tech.*, 22(6):064013, 2009.

[4] John Clarke and A. I. Braginsky, editors. *The SQUID Handbook*, volume 1. Wiley, Weinheim, 2004.

[5] John Clarke and A. I. Braginsky, editors. *The SQUID Handbook*, volume 2. Wiley, Weinheim, 2006.

[6] M. Tinkham. *Introduction to Superconductivity*. Dover, Mineola, NY, 2004.

[7] J.-P. Cleuziou, W. Wernsdorfer, V. Bouchiat, T. Ondarcuhu, and M. Monthioux. Carbon nanotube superconducting quantum interference device. *Nat. Nano.*, 1(1):53–59, 2006.

[8] D. J. Van Harlingen, R. H. Koch, and John Clarke. Superconducting quantum interference device with very low magnetic flux noise energy. *Appl. Phys. Lett.*, 41(2):197–199, 1982.

[9] K. Segall, C. Wilson, L. Li, L. Frunzio, S. Friedrich, M. C. Gaidis, and D. E. Prober. Dynamics and energy distribution of nonequilibrium quasiparticles in superconducting tunnel junctions. *Phys. Rev. B*, 70(21):214520, 2004.

[10] K.K. Likharev. *Dynamics of Josephson Junctions and Circuits*. Gordon and Breach, New York, 1985.

[11] L.S. Kuzmin, K.K. Likharev, V.V. Migulin, E.A. Polunin, and N.A. Simonov. X-band parametric amplifier and microwave squid using single-tunnel-junction superconducting interferometer. In H.D. Hahlbohm and H. Lübbig, editors, *SQUID'85, Superconducting Quantum Interference Devices and Their Applications*, pages 1029–1034. de Gruyter, Berlin, 1985.

[12] J. A. B. Mates, G. C. Hilton, K. D. Irwin, L. R. Vale, and K. W. Lehnert. Demonstration of a multiplexer of dissipationless superconducting quantum interference devices. *Appl. Phys. Lett.*, 92(2):023514, 2008.

[13] R.R. Edelman, J.R. Hesselink, M.B. Zlatkin, and J.V. Crues. *Clinical Manetic Resonance Imaging, 3rd ed.* W.B. Saunders Co, Philadelphia, 2006.

[14] A. Abragam. *The Principles of Nuclear Magnetism.* Oxford Univ. Press, London, 1961.

[15] C.P. Slichter. *Principles of Nuclear Magnetic Resonance, 3rd ed.* Springer-Verlag, New York, 1990.

[16] E.M.R. Haacke, W. Brown, M.R. Thompson, and Venkatesan R. *Magnetic Resonance Imaging: Physical Principles and Sequence Design.* Wiley-Liss, New York, 1999.

[17] X. Hu and D.G. Norris. Advances in high-field magnetic resonance imaging. *Annu. Rev. Biomed. Eng.*, 6:157–184, 2004.

[18] A. Macovski and S.M. Conolly. Novel approaches to low-cost MRI. *Magn. Reson. Med.*, 30:221–230, 1993.

[19] R.D. Venook, N.I. Matter, M. Ramachandran, S.E. Ungersma, G.E. Gold, N.J. Giori, A. Macovski, G.C. Scott, and S.M. Conolly. Prepolarized magnetic resonance imaging around metal orthopedic implants. *Magn. Reson. Med.*, 56:177–186, 2006.

[20] John Clarke, M. Hatridge, and M. Moessle. SQUID-detected magnetic resonance imaging in microtesla fields. *Annu. Rev. Biomed. Engr.*, 9:389–413, 2007.

[21] W. Myers, D. Slichter, M. Hatridge, S. Busch, M. Moessle, R. McDermott, A. Trabesinger, and John Clarke. Calculated signal-to-noise ratio of MRI detected with SQUIDs and faraday detectors in fields from 10 μT to 1.5 T. *Journ. Mag. Reson.*, 86(2):182 – 192, 2007.

[22] J.P. Stack, N.M. Antoun, J.P. Jenkins, R. Metcalfe, and I. Isherwood. Gadolinium-DTPA as a contrast agent in magnetic resonance imaging of the brain. *Neuroradiology*, 30:145–154, 1988.

[23] S.H. Koenig and R.D. III Brown. Relaxation of tissue. In R.K. Gupta, editor, *NMR Spectroscopy of Cells and Organism, Vol. II*, pages 75–114. CRC Press, Boca Raton, 1987.

[24] J. Kurhanewicz, D. Vigneron, P. Carroll, and F. Coakley. Multiparametric magnetic resonance imaging in prostate cancer: present and future. *Curr. Opin. Urol.*, 18:71–77, 2008.

[25] M. Moessle, S.-I. Han, W.R. Myers, S.-K. Lee, N. Kelso, M. Hatridge, A. Pines, and J. Clarke. SQUID-detected microtesla MRI in the presence of metal. *Journ. of Magn. Reson.*, 179:146–151, 2006.

[26] M.N. Leuenberger and D. Loss. Quantum computing in molecular magnets. *Nature*, 410:789, 2001.

[27] J. Tejada, E.M. Chudnovsky, E. del Barco, J.M. Hernandez, and T.P. Spiller. Magnetic qubits as hardware for quantum computers. *Nanotechnology*, 12:181, 2001.

[28] J. Gallop, P.W. Josephs-Franks, J. Davis, L. Hao, and J. Macfarlane. Miniature dc SQUID devices for detection of single atomic spin-flip. *Physica C*, 368:109, 2002.

[29] S.K.H. Lam and D.L. Tilbrook. Development of a niobium nano-SQUID for the detection of small spin populations. *Appl. Phys. Lett*, 82:1078, 2003.

[30] D. Gatteschi, R. Sessoli, and J. Villan. *Molecular Nanomagnets*. Oxford University Press, 2006.

[31] A.G.P. Troeman, H. Derking, B. Borger, J. Pleikies, D. Veldhuis, and H. Hilgenkamp. NanoSQUIDs based on niobium constrictions. *Nano Lett.*, 7:2152, 2007.

[32] C Granata, E Esposito, A Vettoliere, L Petti, and M Russo. An integrated superconductive magnetic nanosensor for high-sensitivity nanoscale applications. *Nanotechnology*, 19(27):275501, 2008.

[33] M Faucher, P O Jubert, O Fruchart, W Wernsdorfer, and V Bouchiat. Optimizing the flux coupling between a nanosquid and a magnetic particle using atomic force microscope nanolithography. *Superconductor Science and Technology*, 22(6):064010 (5pp), 2009.

[34] E. del Barco, A. D. Kent, E. C. Yang, and D. N. Hendrickson. Quantum superposition of high spin states in the single molecule magnet ni_4. *Phys. Rev. Lett.*, 93(15):157202, 2004.

[35] M. Jamet, V. Dupuis, P. Mélinon, G. Guiraud, A. Pérez, W. Wernsdorfer, A. Traverse, and B. Baguenard. Structure and magnetism of well defined cobalt nanoparticles embedded in a niobium matrix. *Phys. Rev. B*, 62(1):493–499, Jul 2000.

[36] D.G. Nishimura. *Principles of Magnetic Resonance Imaging*. Stanford University, 1996.

[37] S.-K. Lee, M. Moessle, W.R. Myers, N. Kelso, A.H. Trabesinger, A. Pines, and John Clarke. SQUID-detected MRI at 132 μT with T_1- weighted contrast established at 10 μT - 300 mT. *Magn. Reson. Med.*, 53:9–14, 2005.

[38] B. Halle. Molecular theory of field-dependent proton spin-lattice relaxation in tissue. *Magn. Reson. Med.*, 56:60–72, 2006.

[39] F.V. Chávez and B. Halle. Molecular basis of water proton relaxation in gels and tissue. *Magn. Reson. Med.*, 56:73–81, 2006.

[40] S.E Ungersma, N.I Matter, J.W Hardy, R.D. Venook, A. Macovski, S.M. Conolly, and G.C. Scott. Magnetic resonance imaging with T_1 disperson constrast. *Magn. Reson. Med.*, 55:1362–1371, 2006.

[41] N.I. Matter, G.C. Scott, R.D. Venook, S.E. Ungersma, T. Grafendorfer, A. Macovski, and S.M. Conolly. Three-dimensional prepolarized magnetic resonance imaging using rapid acquisition with relaxation enhancement. *Magn. Reson. Med.*, 56:1085–1095, 2006.

[42] H.C. Seton, J.M.S. Hutchinson, and D.M. Bussel. A 4.2 K receiver coil and SQUID amplifier used to improve the SNR of low-field magnetic resonance images of the human arm. *Meas. Sci. Tech.*, 8:198–207, 1997.

[43] W.R. Myers, M. Moessle, and John Clarke. Correction of concomitant gradient artifacts in experimental microtesla MRI. *Jour. Magn. Reson.*, 177:274–284, 2005.

[44] H.C. Seton, D.M. Bussell, and J.M.S. Hutchison. Liquified Gas Cryostat. UK Patents GB2331798 and GB2351549.

[45] F. Wellstood, C. Heiden, and John Clarke. Integrated dc SQUID magnetometer with a high slew rate. *Rev. Sci. Inst.*, 55:952–957, 1984.

[46] W.R. Myers. *Potential Applications of Microtesla Magnetic Resonance Imaging Detected Using Superconducting Quantum Interference Device*. PhD thesis, University of California, Berkeley, 2006.

[47] J.E. Zimmerman. SQUID instruments and shielding for low-level magnetic measurements. *Journ. Appl. Phys.*, 48:702–710, 1977.

[48] G. Stroink, B. Blackford, B. Brown, and M. Horacek. Aluminum shielded room for biomagnetic measurements. *Rev. Sci. Instrumen.*, 52:463–468, 1981.

[49] S. Fahy, C. Kittel, and S.G. Louie. Electromagnetic screening by metals. *Am. J. Phys.*, 56:989–992, 1988.

[50] J.R. Clem. Johnson noise from normal metal near a superconducting SQUID gradiometer circuit. *IEEE Trans. Magn.*, 23:1093–1096, 1986.

[51] N.I. Matter, G.C. Scott, T. Grafendorfer, A. Macovski, and S.M. Conolly. Rapid polarizing field cycling in magnetic resonance imaging. *IEEE Trans. Med. Imag.*, 25:84–93, 2006.

[52] D.M. Pozar. *Microwave Engineering*. Addison-Wesley Publishing Co., Reading, MA, 1990.

[53] J.R. Moser. Low-frequency low-impedance electromagnetic shielding. *IEEE Trans. Elect. Comp.*, 30:202–210, 1988.

[54] A. Lupaşcu, E. F. C. Driessen, L. Roschier, C. J. P. M. Harmans, and J. E. Mooij. High-contrast dispersive readout of a superconducting flux qubit using a nonlinear resonator. *Phys. Rev. Lett.*, 96(12):127003, 2006.

[55] I. Siddiqi, R. Vijay, M. Metcalfe, E. Boaknin, L. Frunzio, R. J. Schoelkopf, and M. H. Devoret. Dispersive measurements of superconducting qubit coherence with a fast latching readout. *Phys. Rev. B*, 73(5):054510, 2006.

[56] F. Mallet, F. Ong, A. Palacios-Laloy, F. Nguyen, P. Bertet, D. Vion, and D. Esteve. Single-shot qubit readout in circuit quantum electrodynamics. *Nat. Phys.*, 5:791–795, 2009.

[57] R. Vijay, J. D. Sau, Marvin L. Cohen, and I. Siddiqi. Optimizing anharmonicity in nanoscale weak link josephson junction oscillators. *Phys. Rev. Lett.*, 103(8):087003, Aug 2009.

[58] R. Vijay, M. H. Devoret, and I. Siddiqi. Invited review article: The josephson bifurcation amplifier. *Rev. Sci. Inst.*, 80(11):111101, 2009.

[59] M. J. Feldman, P. T. Parrish, and R. Y. Chiao. Parametric amplification by unbiased Josephson junctions. *Journ. Appl. Phys.*, 46(9):4031–4042, 1975.

[60] B. Yurke, L. R. Corruccini, P. G. Kaminsky, L. W. Rupp, A. D. Smith, A. H. Silver, R. W. Simon, and E. A. Whittaker. Observation of parametric amplification and deamplification in a Josephson parametric amplifier. *Phys. Rev. A*, 39(5):2519–2533, 1989.

[61] R. Vijay. *Josephson Bifurcation Amplifier: Amplifying quantum signals using a dynamical bifurcation*. PhD thesis, Yale University, 2008.

[62] M. I. Dykman and M. A. Krivoglaz. Fluctuations in non-linear systems near bifurcations corresponding to the appearance of new stable states. *Physica A*, 104(3):480–494, 1980.

[63] M. Castellanos-Beltran, K. D. Irwin, G. C. Hilton, L. R. Vale, and K. W. Lehnert. Amplification and squeezing of quantum noise with a tunable josephson metamaterial. *Nat Phys*, 4(12):929–931, print 2008. M3: 10.1038/nphys1090; 10.1038/nphys1090.

[64] N. Bergeal, F. Schackert, M. Metcalfe, R. Vijay, V.E. Manucharyan, L. Frunzio, D.E. Prober, R. J. Schoelkopf, S.M. Girvin, and M.H. Devoret. Phase preserving amplification near the quantum limit with a Josephson ring modulator, 2009.

[65] Carlton M. Caves. Quantum limits on noise in linear amplifiers. *Phys. Rev. D*, 26(8):1817–1839, 1982.

[66] V. E. Manucharyan, E. Boaknin, M. Metcalfe, R. Vijay, I. Siddiqi, and M. Devoret. Microwave bifurcation of a Josephson junction: Embedding-circuit requirements. *Phys. Rev. B*, 76(1):014524, 2007.

[67] D.H. Slichter, O. Naaman, and I. Siddiqi. Millikelvin thermal and electrical performance of lossy transmission line filters. *Appl. Phys. Lett.*, 94:192508, 2009.

[68] P. H. Bryant, R. Movshovich, and B. Yurke. Noise rise in nondegenerate parametric amplifiers. *Phys. Rev. Lett.*, 66(20):2641–2644, 1991.